

On the origin of a phosphate enriched interval in the Chattanooga Shale (Upper Devonian) of Tennessee—A combined sedimentologic, petrographic, and geochemical study



Yifan Li ^{a,b,*}, Juergen Schieber ^b

^a School of Energy Resources, China University of Geosciences (Beijing), Beijing, 100083, China

^b Department of Geological Sciences, Indiana University, Bloomington, IN 47403, USA

ARTICLE INFO

Article history:

Received 24 June 2015

Received in revised form 3 September 2015

Accepted 6 September 2015

Available online 24 September 2015

Editor: Dr. B. Jones

Keywords:

Late Devonian

Chattanooga shale

Phosphatic interval

Reworking & winnowing events

North America

ABSTRACT

The Devonian Chattanooga Shale contains an uppermost black shale interval with dispersed phosphate nodules. This interval extends from Tennessee to correlative strata in Kentucky, Indiana, and Ohio and represents a significant period of marine phosphate fixation during the Late Devonian of North America. It overlies black shales that lack phosphate nodules but otherwise look very similar in outcrop. The purpose of this study is to examine what sets these two shales apart and what this difference tells us about the sedimentary history of the uppermost Chattanooga Shale.

In thin section, the lower black shales (PBS) show pyrite enriched laminae and compositional banding. The overlying phosphatic black shales (PhBS) are characterized by phosbioclasts, have a general banded to homogenized texture with reworked layers, and show well defined horizons of phosphate nodules that are reworked and transported. In the PhBS, up to 8000 particles of P-debris per cm² occur in reworked beds, whereas the background black shale shows between 37–88 particles per cm². In the PBS, the shale matrix contains between 8–16 phosphatic particles per cm². The shale matrix in the PhBS contains 5.6% inertinite, whereas just 1% inertinite occurs in the PBS. The shale matrix in both units is characterized by flat REE patterns (shale-normalized), whereas Phosbioclast-rich layers in the PhBS show high concentrations of REEs and enrichment of MREEs. Negative Ce-anomalies are common to all samples, but are best developed in association with Phosbioclasts. Redox-sensitive elements (Co, U, Mo) are more strongly enriched in the PBS when compared to the PhBS. Trace elements associated with organic matter (Cu, Zn, Cd, Ni) show an inverse trend of enrichment. Deposited atop a sequence boundary that separates the two shale units, the PhBS unit represents a transgressive systems tract and probably was deposited in shallower water than the underlying PBS interval. The higher phosphate content in the PhBS is interpreted as the result of a combination of lower sedimentation rates with reworking/winnowing episodes. Three types of phosphatic beds that reflect different degrees of reworking intensity are observed. Strong negative Ce anomalies and abundant secondary marcasite formation in the PhBS suggests improved aeration of the water column, and improved downward diffusion of oxygen into the sediment. The associated oxidation of previously formed pyrite resulted in a lowering of pore water pH and forced dissolution of biogenic phosphate. Phosphate dissolution was followed by formation of secondary marcasite and phosphate. Repeated, episodic reworking caused repetitive cycles of phosphatic dissolution and reprecipitation, enriching MREEs in reprecipitated apatite. A generally “deeper” seated redox boundary favored P-remineralization within the sediment matrix, and multiple repeats of this process in combination with wave and current reworking at the seabed led to the formation of larger phosphatic aggregates and concentration of phosphate nodules in discrete horizons.

© 2015 Elsevier B.V. All rights reserved.

1. Introduction

The formation of sedimentary phosphate deposits is still debated for specific instances (e.g., Follmi, 1996; Trappe, 1998; Kouchinsky et al., 1999; Schulz and Schulz, 2005; Dornbos, 2011; Bailey et al., 2013).

* Corresponding author at: School of Energy Resources, China University of Geosciences (Beijing), Beijing, 100083, China.

E-mail address: yifangeosci@gmail.com (Y. Li).

Although upwelling has been considered as an important factor for P-supply along continental margins for modern phosphatic sediments (e.g., Kazakov, 1937; Burnett, 1977; Baturin, 1982), mechanisms that produce phosphate-rich sediments without upwelling have also been recognized (e.g., Heggie et al., 1990; O'brien et al., 1990). Hydrothermal processes or submarine volcanic activity have been proposed as additional factors for sedimentary phosphate enrichment (Berner, 1973; Froelich et al., 1982; Wheat et al., 1996; Petsch and Berner, 1998).

Recent studies show abundant evidence of microbial mediation and even direct evidence of microbial colonies in the sediment (Reimers et al., 1990; Kouchinsky et al., 1999; Schulz and Schulz, 2005; Bailey et al., 2007; Barale et al., 2013; Lepland et al., 2013). In modern and ancient sediments, (Kazakov, 1937; Burnett, 1977), giant sulfur-oxidizing bacteria, such as *Thiomargarita*, *Beggiatoa*, and *Thioploca*, which are abundant in phosphogenic settings may play an important role in phosphogenesis by storing phosphate under oxic conditions and releasing large amounts of dissolved phosphate in anoxic conditions to facilitate rapid apatite precipitation (e.g., Reimers et al., 1990; Schulz and Schulz, 2005). It has also been demonstrated that bacterially mediated phosphogenesis can rapidly permineralize sulfide-oxidizing bacteria and others types of organic remains (Bailey et al., 2007; Bailey et al., 2013; Lepland et al., 2013). Yet whereas these microbial pathways are probably essential for mobilizing and redistributing phosphate in surficial sediments, observations from both modern and ancient phosphorites implicate low sedimentation rates, strong bottom currents, and an abundance of organic matter as essential ingredients for the formation of phosphorites (Heggie et al., 1990; O'brien et al., 1990; Follmi, 1996; Baturin, 1999). The microbially driven decay of organic matter releases phosphate to pore waters, and contributes to supersaturation that leads to phosphogenesis (Baturin, 1999). Strong bottom currents mechanically remobilize and transport existing phosphatic particles, and in alternation with “resting periods” during which chemical processes concentrate phosphate (e.g., Follmi, 1996; Baturin, 1999; Dornbos et al., 2006; Follmi et al., 2007; Dickinson and Wallace, 2009) phosphate enrichment proceeds in repetitive cycles of reworking and redeposition.

The phosphatic interval of the Upper Devonian Chattanooga Shale and its lateral equivalents in Tennessee, Kentucky, Indiana and Ohio and are considered the result of deposition during a major transgression in the Late Devonian of the eastern US (e.g., Schieber, 1998; Lazar, 2007) (Figs. 1, 2, 3). In spite of extensive research on the Devonian black shales of the eastern US (Roen, 1983) and basic study about the Upper Devonian phosphate nodules (Acomb, B., 1979), phosphate formation in these shales has only received scant attention. In this study we endeavor to

better understand the conditions that caused strong phosphate enrichment in this unit through cm to mm scale petrographic examination, quantitative analysis of the distribution of phosphatic debris, geochemical analysis, and detailed optical microscopy and SEM observations. Besides microbial mediation and decay of organic matter, dissolution of phosphatic fossil debris due to fluctuation of the redox boundary and pH levels may have played an important role in the phosphogenesis of these sediments.

2. Geological setting

The Upper Devonian Chattanooga Shale is part of a thin, epicontinental black shale sequence of Late Devonian age that was deposited over large portions of the North American craton (de Witt et al., 1993) (Fig. 1). It is equivalent to the New Albany Shale in the Illinois Basin and the Ohio Shale in the central and northern Appalachian Basin. Unconformably overlying a range of older strata, the Chattanooga Shale was subdivided into three members: the lowermost Hardin Sandstone (only found in the southwestern Tennessee), the Dowlstown Member, and the uppermost Gassaway Member (Conant and Swanson, 1961). At Chestnut Mound in central Tennessee, only the latter two members occur (Fig. 2). Although the Chattanooga Shale has been considered as the deposit of a deep stagnant basin (Potter et al., 1982; Etensohn, 1985), recent studies show that it was probably deposited in comparatively shallow water and was affected by storm waves and episodic erosive events (Schieber, 1994a; Schieber, 1994b; Schieber, 1998). Erosive events of variable strength and duration are indicated by erosion surfaces beneath which from a few centimeters to more than a meter of section is missing. Storm-wave induced hummocky cross-stratified sand/silt beds, and mud tempestites indicate that the seafloor was close to or within reach of storm waves (Schieber, 1994a). Subtle but widespread bioturbation features imply that bottom waters were rarely anoxic, but instead variably oxygen restricted (Schieber, 1994a; Schieber, 2003; Schieber, 2009).

The study interval is in the upper portion of the Gassaway Member, an interval that is subdivided into a lower, middle, and upper unit. The

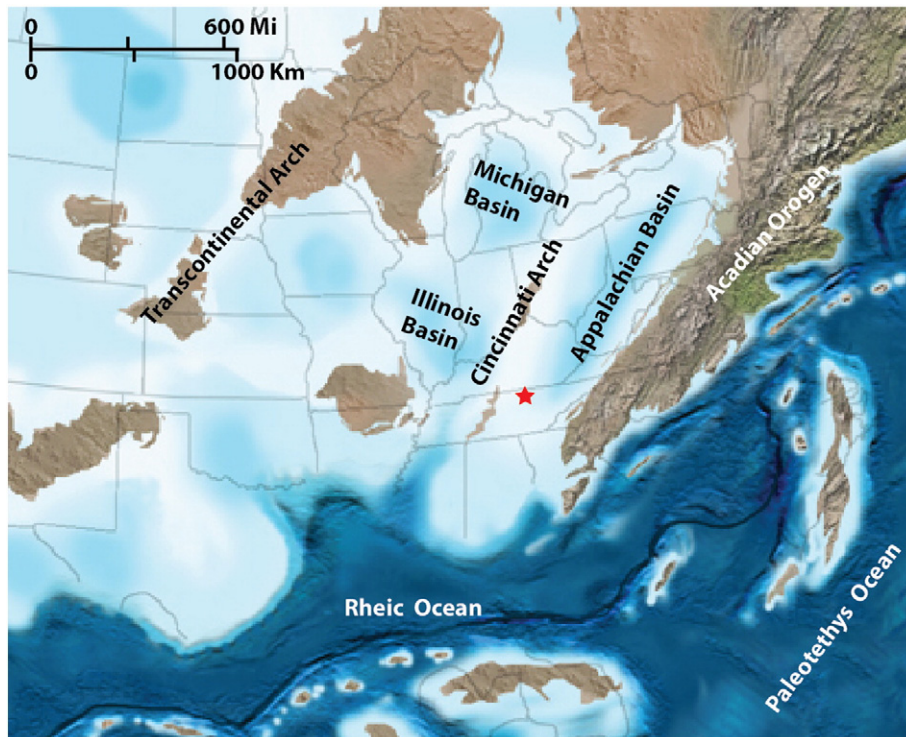


Fig. 1. Late Devonian paleogeographic map of Eastern North America (360 Ma) modified after (Blakey, 2005) and location of study site (red star). Various structural elements are indicated. The Chestnut Mound exposure is located 500 m west of the Chestnut Mound (TN) post office on the east side of US Highway 70 N.

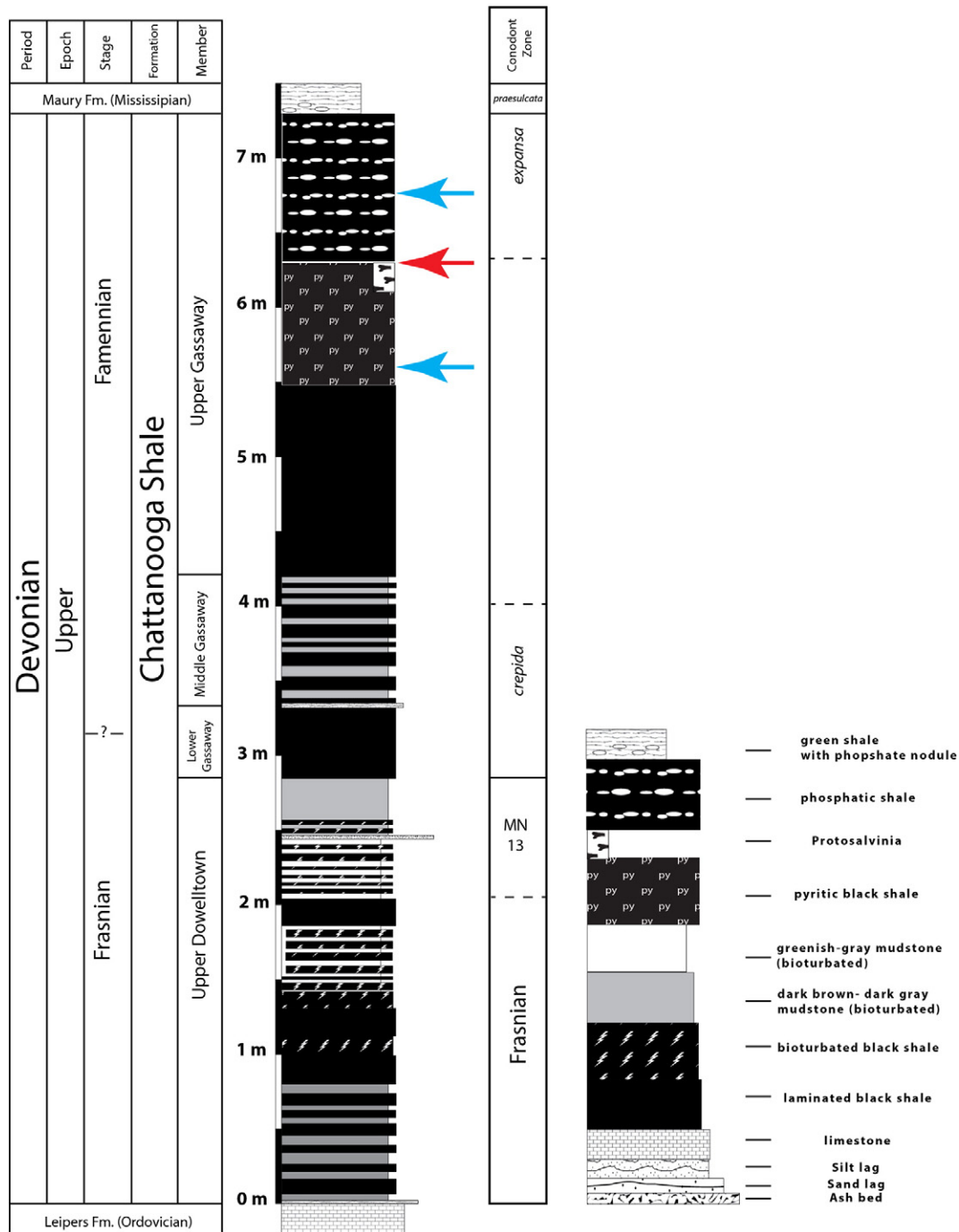


Fig. 2. Lithostratigraphy of the Chattanooga Shale succession found in Chestnut Mound Tennessee. Conodont data are based on Over (2007). Two blue arrows indicate bottom and top of target section. A red arrow marks the described erosion surface in the target section.

upper unit consists predominantly of resistant weathering black shales that show fine internal laminae thought to reflect bedload transport and bottom currents (Schieber et al., 2007), as well as current reworked pyritic beds (Schieber and Baird, 2001). At the very top of the Upper Gassaway member a phosphatic interval with current reworked phosphate nodules occurs. This interval, the focus of this study, has in places been removed by post-Devonian erosion, but its distribution suggests that it once was an extensive blanket of phosphatic shale. It is characterized by a relative abundance of phosphatic fossil debris (fishbone, fish scales, phosphatic brachiopods, and conodonts), as well as fossilized wood debris and other biogenic particles. *Tasmanites* cysts, the remains of fossil of alga, are common. The biostratigraphic

marker *Protosalvinia*, a likely plant fossil (Over et al., 2009), occurs in the upper portion of the upper Gassaway Member (Schieber, 1998) and at Chestnut Mound it is found just beneath the erosion surface that separates the phosphatic shale (PhBS) interval from the underlying pyritic (PBS) shales (Fig. 2).

A sequence stratigraphic subdivision of the Chattanooga Shale and its lateral equivalents have been developed through tracing of laterally extensive erosion surfaces (Schieber, 1998; Schieber and Lazar, 2004; Lazar, 2007; Schieber et al., 2010) and further confirmed through conodont data from Over (2007) and Over et al. (2009) and the position of the *Protosalvinia* interval (Over et al., 2009) within measured stratigraphic sections. At Chestnut Mound multiple sequences and system



Fig. 3. (A) Lithostratigraphic overview of the Chattanooga Shale in Chestnut Mound. (B) Location and contact relationship between the PhBS (phosphatic black shale) and PBS (pyritic black shale) units. Yellow dashed line marks the boundary between these two units. (C) Distribution of phosphate nodules within the PhBS unit. Yellow arrows point to phosphate nodules. Yellow dashed lines mark phosphate nodule layers. (D) Image of a sliced sample across the PBS/PhBS contact (CM-K5). Yellow arrow points to a phosphate nodule that occurs within a phosphobioclast layer that overlies the contact. White streaks (white arrow) are late diagenetic calcite veins.

tracts have been identified (Schieber, 1998; Schieber and Lazar, 2010). The PBS and PhBS intervals are separated by an erosion surface that is interpreted as a sequence boundary, and are interpreted to represent a highstand systems tract (HST) and a transgressive systems tract (TST) respectively. A phosphatic lag occurs above this erosion surface (Fig. 3B). According to conodont data from this location (Over, 2007), the PhBS interval falls into the middle *expansa* zone (Fig. 2), which is equivalent to the miospore zones from *Rugospora versabilis*–*Grandispora cornuta* (VCo) to *Retispora lepidophyta*–*Knoxisporites literatus* (LL) (Streel et al., 2000; Isaacson et al., 2008). This interval correlates to a transgression in the lower half of T–R cycle II of the global Devonian sea level curve (Johnson and Sandberg, 1989; Johnson et al., 1989; Johnson et al., 1991; Sandberg et al., 2002; Kaufmann, 2006). The timing of this cycle does not coincide temporally with postulated glacial events near the Devonian–Mississippian boundary. Subsequent glacial event occurred during the miospore zones from *Retispora lepidophyta*–*Indotriradites explanatus* (LE) to *Retispora lepidophyta*–*Verrucosporites nitidus* (LN) (Brezinski et al., 2008; Caputo et al., 2008; Brezinski et al., 2009). It coincides temporally with the overlying Maury Formation (Fig. 2) that contains *praesulcata* conodonts, and occurred approximately 2 million years later (Kaufmann, 2006).

3. Materials and methods

The thickness of our target section that traverses the contact between pyritic black shales and phosphatic black shales is 1.2 m

(Fig. 2). Ten samples were selected for preparation of polished thin sections. Samples CM-K1 to CM-K5 were selected from the PhBS interval, and samples CM-K6 to CM-J2 were collected from the PBS interval. These polished thin sections were examined under the optical microscope (transmitted and reflected light) and the scanning electron microscope (SE and BSE imaging). Subsamples from CM-K2, CM-K4 and CM-K5 were polished by argon ion milling for high resolution SEM imaging. Examination of organic macerals was conducted in the coal laboratory of the Indiana Geological Survey under supervision of Dr. Maria Mastalerz. The distribution of phosphatic debris in thin sections was quantified by point counting cm-thick intervals of “background” black shale, as well as phosphatic lag deposits. Although shale and mudstone are both widely used terms for fine grained sediments, because of the historical use of the term “shale” in the stratigraphic designation (Chattanooga Shale), and also for simplicity, we will primarily use the term shale in this contribution, with the understanding that it includes what some prefer to identify as mudstones.

Sub-samples of “background shale”, avoiding pyritic or phosphate enriched layers, were cut out of the larger samples and analyzed for major elements, trace elements, carbon and sulfur. In sample CM-K4, a phosphobioclast layer (labeled CM-K4b) was cut out and analyzed for major and rare earth elements. Geochemical analyses were conducted at Acme laboratories (Vancouver, Canada), using X-ray fluorescence (XRF) and Inductively Coupled Plasma–Mass Spectrometry (ICP-MS). Carbon and sulfur concentrations were determined with a Leco elemental analyzer. Rare earth elements (REE) were normalized against

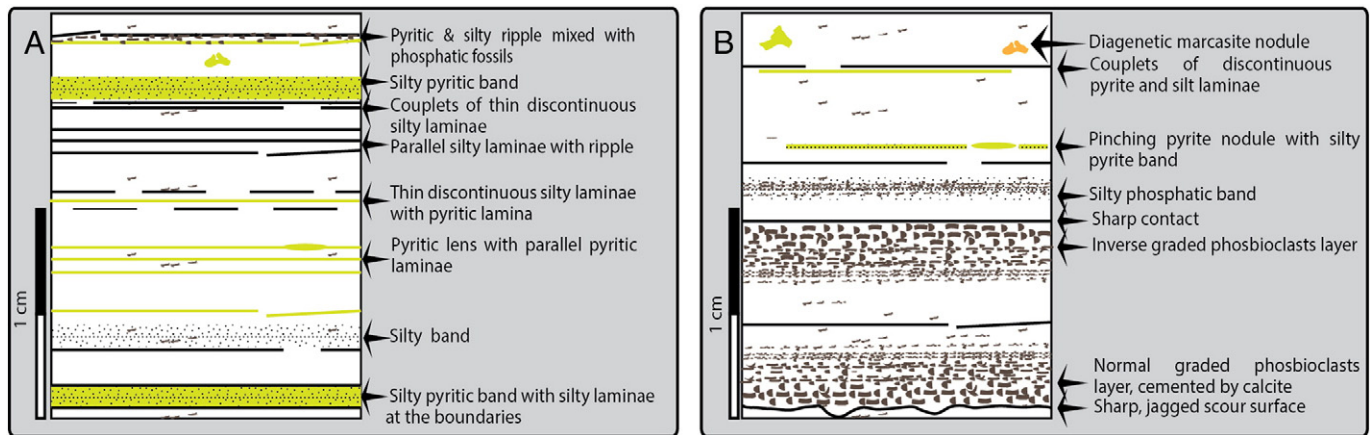


Fig. 4. (A) Line drawing of sedimentary features in the PBS unit (matrix rendered white for better visibility). (B) Line drawing of sedimentary features in the PhBS unit (matrix rendered white for better visibility).

Post-Archean Australian Shale (PAAS) (Taylor and McLennan, 1985; McLennan, 1989) and Eu/Eu^* , Ce/Ce^* were calculated using published formulae (see below; (Taylor and McLennan, 1985):

$$\text{Eu}/\text{Eu}^* = \text{Eu}_N / (\text{Sm}_N * \text{Gd}_N)^{1/2}$$

$$\text{Ce}/\text{Ce}^* = \text{Ce}_N / (\text{La}_N * \text{Pr}_N)^{1/2}$$

4. Description and geochemical results

4.1. Shale facies

Two types of shale facies occur in the upper part of the Upper Gassaway: the lower pyritic black shale (PBS) and the upper phosphatic black shale (PhBS) (Figs. 3B, 4).

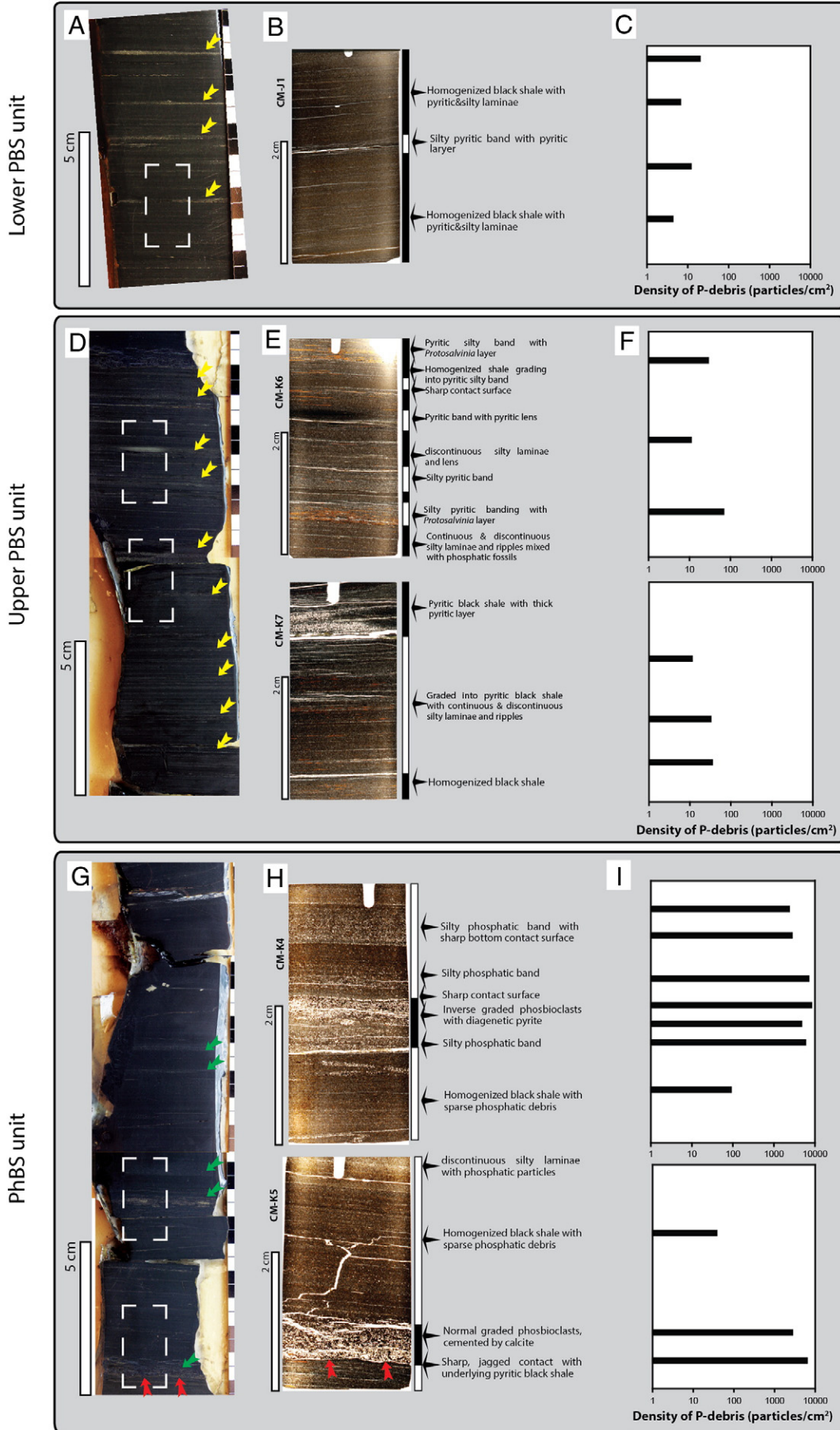
The PBS unit (0.8 m thick) is characterized by pyrite enriched laminae and compositional banding (Figs. 4A, 5). The term compositional banding implies mm-scale layers (bands) of variable composition that lack sharp boundaries and grade into each other. In the lower portion of the PBS unit compositional banding is accentuated by varying abundance of pyrite framboids between in alternate bands, scattered pyritic nodules (0.5–2 mm), highly pyrite enriched layers (0.5–3 cm thick) that consist of pyritized fecal pellets and the pyritic infills of *Tasmanites* cysts (Schieber, 1998; Schieber and Baird, 2001), and in places continuous to discontinuous silt laminae (Fig. 5A, B). The upper portion of the PBS unit generally shows a greater abundance of silt laminae that are interstratified with banded pyritic shales (Fig. 5D, E). Compositional banding is accentuated by variable abundance of Fe-sulfides, occurring as pyrite framboids, as well as grains of euhedral pyrite and marcasite. Phosphatic fossil fragments (conodonts, fish bones and brachiopods) are sparsely scattered through the black shale matrix (Fig. 6A). Reworked laminae can contain more phosphatic debris and the debris may show variable degrees of pyritization (Fig. 6B). Collapsed *Tasmanites* cysts are abundant throughout the PBS interval. In the uppermost 20 cm of the interval compressed remains of the plant fossil *Protosalvinia* (Over et al., 2009) are common on bedding planes (Fig. 5E, CM-K6). A variety of organic macerals was observed in thin sections and was quantified via point

counting. Recognized organic components are alginite (3.6%), amorphinite (13.2%), liptodetrinite (7.4%), vitrinite (0.8%), inertinite (1%), and bitumen (0.2%) (Fig. 7A).

In the lower part of the PBS interval (thin sections CM-J1 and CM-J2) the abundance of phosphatic particles averages 9 particles per cm^2 in background black shale (Figs. 5C, 6A). Reworked silt laminae become more abundant in the upper portion of the PBS interval, and this change is accompanied by an increase in phosphatic debris (Figs. 5D, E, F, 6B). Silt laminae bearing portions of thin sections (CM-K8, CM-K7, CM-K6) average 43 phosphatic particles per cm^2 , and background black shale in these thin sections averages 14 phosphatic particles per cm^2 (Fig. 5F).

The overlying PhBS interval is characterized by a relative (to PBS) enrichment with biogenic phosphate debris in the background shale and abundant phosphate nodules (Fig. 4B). The lower part of the PhBS interval is characterized by phosbioclasts and silty bands with phosphatic debris (Figs. 4B, 6G, H). At the base of the PhBS unit, a normally graded lag deposit with abundant phosbioclasts and a sharp, jagged basal scour surface is observed. In places within the lower PhBS unit inversely graded layers with phosbioclasts and reworked pyrite occur (Fig. 5G, H). Silty phosphatic bands consist mainly of detrital quartz and phosphatic fossil debris, may be homogenous, or show hints of normal or inverse grading (Figs. 4B, 5G, H). Scattered through the black shale matrix are thin, continuous to discontinuous, silty and variably pyritic laminae (Fig. 5H). Aside of phosphatic lags and silty phosphatic bands and laminae (Fig. 6C, E, F), phosphatic debris is relatively sparse in the “background” black shale (Fig. 6D, H). Phosphate nodules (1–20 cm in size) occur within horizons that are characterized by phosbioclast-rich lags and/or silty phosphatic bands (Fig. 3C, D). In places pyritic laminae and small pyrite nodules occur, but they are much less abundant than in the PBS interval. Compared with the PBS unit, framboidal pyrite and micron-size euhedral pyrite grains are less abundant in the “background” black shale, but still can form localized concentrations in thin laminae. Many euhedral marcasite grains occur in association with pyrite–marcasite clusters, and remnant spherical shapes suggest degradation (partial dissolution) and deformation of original pyrite framboids. *Tasmanites*, the cysts of marine brown algae (Tappan, 1980) are a common matrix constituent throughout the

Fig. 5. (A) Contrast enhanced image, with common sedimentologic features observed in the lower part of the PBS interval. Dashed rectangles mark locations of thin sections. Yellow arrows point to pyritic layers. (B) Photomicrographs of CM-J1, with associated sedimentary features observed in the lower PBS unit. (C) Density of P-debris in thin sections of CM-J1. (D) Contrast enhanced image, with common sedimentologic features observed in the upper part of the PBS unit. Dashed rectangles mark locations of thin sections. Yellow arrows point to pyritic layers. (E) Photomicrographs of CM-K6 and CM-K7, with associated sedimentary features observed in the upper PBS facies. (F) Density of P-debris in thin sections of CM-K6 and CM-K7. (G) Contrast enhanced image, with common sedimentologic features observed in the PhBS facies. Dashed rectangles mark locations of thin sections. Green arrows point to phosphatic intervals. (H) Photomicrographs of CM-K4 and CM-K5, with associated sedimentary features observed in the PhBS facies. (F) Density of P-debris in thin sections of CM-K4 and CM-K5. Red arrows point to erosive contact between PBS (below) and PhBS (above) unit.



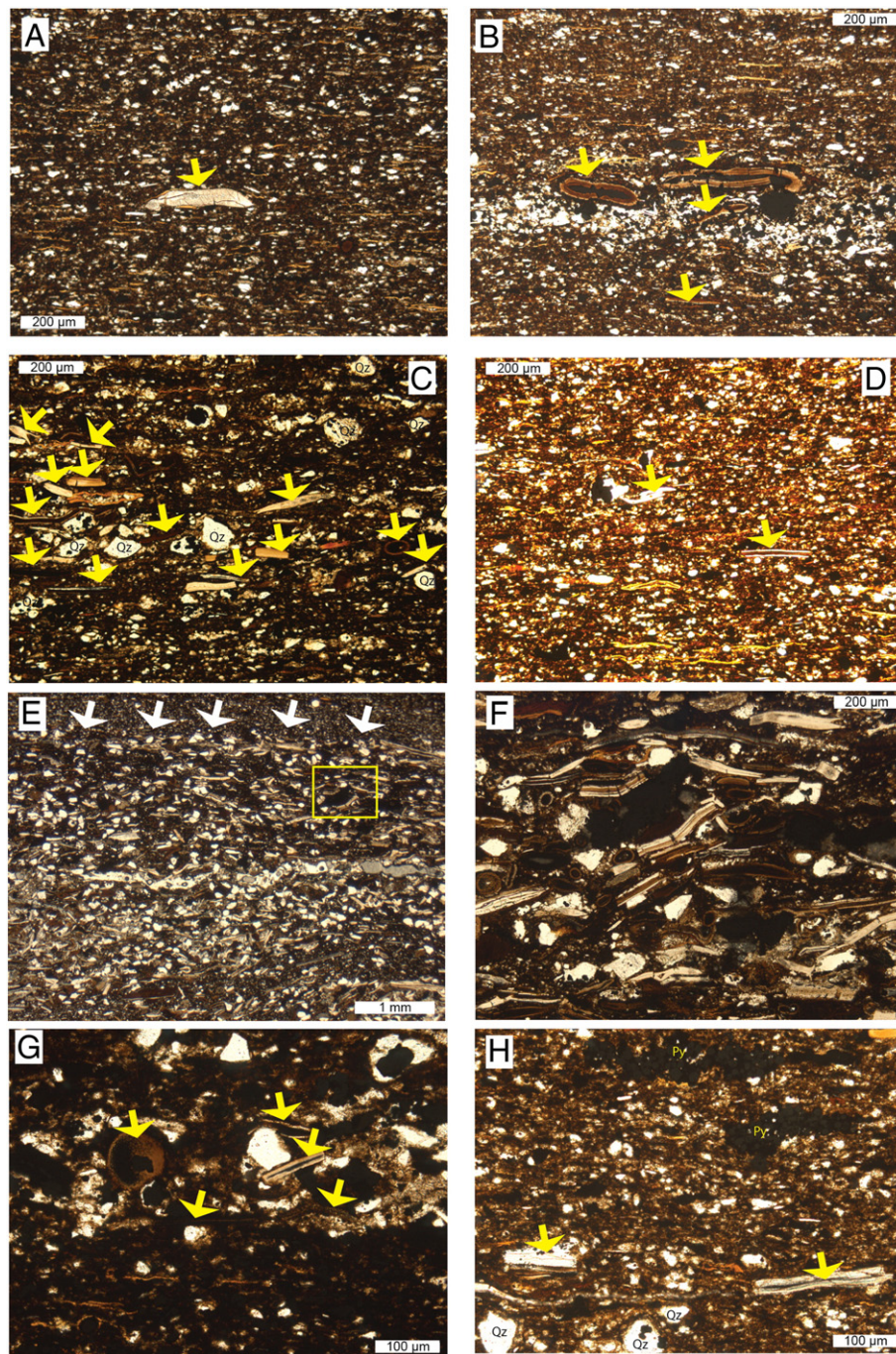


Fig. 6. (A) Phosphatic particles sparsely distributed in homogenized shale of the PBS unit. (B) Phosphatic particles (yellow arrows) are concentrated along silty & pyritic laminae of the PBS unit. (C) Abundant phosphatic fragments are concentrated in silty phosphatic bands of the lower PhBS unit. (D) Phosphatic particles (yellow arrows) are sparsely distributed in homogenized shale of the lower PhBS unit. (E) Phosphatic particles are highly concentrated in a phosbioclast layer in the lower PhBS unit, notice the sharp upper contact (white arrows). (F) Close-up image of phosphatic fossils (dominantly fragments of *Lingula* shells) in a phosbioclast layer in the lower PhBS. (G) Phosphatic particles (yellow arrows) are concentrated along silty laminae in the upper section of PhBS unit. (H) Sparsely distributed phosphatic fossil debris (yellow arrows) in homogenized shale of the upper PhBS unit.

lower portion of the PhBS facies. Organic macerals include 7.2% alginite, 18.2% amorphinite, 5.4% liptodetrinite, 2.2% vitrinite, 5.6% inertinite, and 0.8% bitumen (Fig. 7B).

Phosphatic fossil debris is significantly more abundant in the PhBS interval when compared to the PBS interval. Reworked phosbioclast layers may contain as many as 8000 pieces of phosphatic fossil debris per cm², and silty phosphatic bands average 2500 particles per cm² (Fig. 5I). In contrast, in the background black shale the abundance of phosphatic particles averages 60 particles per cm² (Fig. 5I).

4.2. Geochemistry results

The abundances of major chemical constituents are listed in Table 1. Except for sample CM-K4b, a layer highly enriched in phosbioclasts, results of all samples (selected from the black shale matrix) are plotted in Fig. 8. The SiO₂ content (Fig. 8) of the PhBS interval, ranging from 50.41 wt.% to 52 wt.%, is consistently higher than that of the PBS interval (44.09 wt.% to 46.31 wt.%). Similarly, Al₂O₃ is enriched in the PhBS interval (11.06–12.16 wt.%) relative to the PBS interval (Fig. 8). Except for

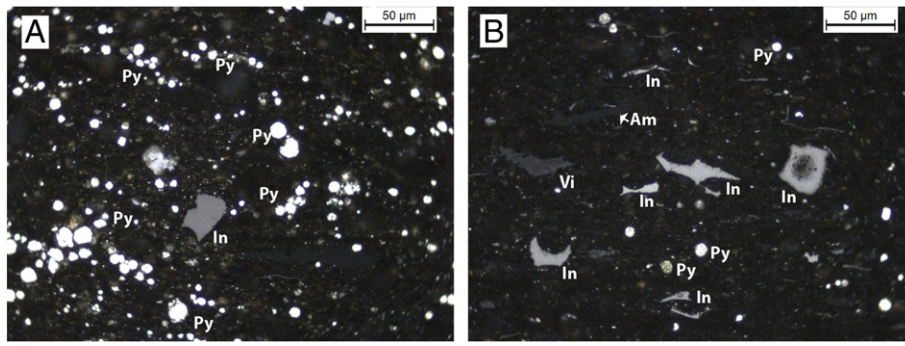


Fig. 7. (A) Inertinite (In) in the “background” shale of the PBS unit. (B) Inertinite (In) and other organic particles in the “background” shale of the PhBS unit. In = Inertinite, Py = pyrite, Vi = vitrinite, Am = amorphinite.

sample CM-K4b (phosbioclast layer, 6.78 wt.% P₂O₅), the P₂O₅ content of the PhBS interval shows maximum enrichment in sample CM-K4 (abundant silty phosphatic bands, 1.71 wt.% P₂O₅), but samples of background black shale show no systematic difference in P₂O₅ content between PBS and PhBS units (Fig. 8). Of course, once the nodules and phosbioclast layers are added, P₂O₅ enrichment in the PhBS interval is quite obvious. Because the analyzed samples were selected with a view toward characterization of background sedimentation, the P₂O₅ content of this interval is not reflected in the analyses shown in Table 1 and Fig. 8. The estimated proportions of phosphate nodules,

phosbioclast layers and silty phosphatic bands that are observed in outcrop within the PhBS interval are respectively ~5 vol.%, ~10 vol.%, and ~15 vol.%. Based on our data we assume average P₂O₅ contents of phosbioclast layers and silty phosphatic bands at 6.5 wt.% and 1.5 wt.%, respectively, and assume an apatite dominated composition with 40 wt.% P₂O₅ for the nodules. When added to the average P₂O₅ content of background PhBS (0.27 wt.%), the estimated average P₂O₅ content for the PhBS interval should be approximately 3 wt.%, about an order of magnitude larger than observed in the PBS interval (0.27 wt.%) (Fig. 8). The abundance of total Fe₂O₃ starkly differs between the PBS

Table 1
Geochemical results of samples from uppermost Chattanooga Shale at Chestnut Mound, Central Tennessee.

Elements	Samples											
	CM-K1	CM-K2	CM-K3	CM-K4	CM-K4b	CM-K5	CM-K6	CM-K7	CM-K8	CM-J1	CM-J2	
SiO ₂ (%)	51.86	51.86	50.60	50.41	45.51	52.00	44.66	44.78	44.09	45.78	46.31	
Al ₂ O ₃ (%)	12.08	12.16	12.15	11.06	8.64	12.00	9.73	10.08	10.00	10.50	10.98	
Fe ₂ O ₃ (%)	5.21	4.84	4.29	3.79	4.14	3.29	13.24	11.93	11.82	9.44	10.24	
CaO (%)	0.32	0.49	0.42	2.44	9.88	0.80	0.58	0.94	0.26	0.21	0.15	
MgO (%)	1.52	1.49	1.47	1.27	0.93	1.31	0.94	1.07	0.98	0.95	0.97	
Na ₂ O (%)	0.32	0.29	0.28	0.29	0.47	0.28	0.27	0.27	0.28	0.24	0.25	
K ₂ O (%)	4.27	4.39	4.48	4.17	3.31	4.53	3.62	3.67	3.73	3.92	4.13	
MnO (%)	0.01	0.01	0.01	0.01	0.02	0.01	0.01	0.02	0.01	0.01	0.01	
TiO ₂ (%)	0.70	0.68	0.67	0.66	0.52	0.72	0.60	0.60	0.59	0.63	0.63	
P ₂ O ₅ (%)	0.14	0.30	0.23	1.71	6.78	0.41	0.37	0.57	0.17	0.13	0.10	
Cr ₂ O ₃ (%)	0.018	0.017	0.019	0.021	0.017	0.016	0.007	0.009	0.008	0.008	0.008	
LOI (%)	23.60	23.08	24.96	24.04	19.1	24.80	25.41	25.90	27.88	28.69	26.52	
Ba (ppm)	307	309	339	332	/	376	299	313	348	355	367	
Co (ppm)	12.5	10.5	9.5	10.5	/	11.5	66.1	60.6	53.7	51.5	47.2	
Th (ppm)	9.4	9.9	9.7	13.8	/	10.1	8.1	8.0	7.2	7.6	7.7	
U (ppm)	33.5	37.6	34.4	89.9	/	52.2	69.0	81.8	71.2	63.0	54.2	
V (ppm)	1972	1293	1051	996	/	810	287	253	250	248	219	
Y (ppm)	34.3	49.3	41.9	158.5	625.4	58.6	46.1	55.4	44.1	38.1	30.2	
La (ppm)	33.1	39.3	37.4	105.6	364.3	53.4	46.4	46.6	35.8	37.2	36.0	
Ce (ppm)	56.6	64.7	59.8	166.9	589.1	81.5	72.0	78.7	70.1	70.3	65.5	
Pr (ppm)	7.56	9.66	8.53	31.17	122.43	12.41	9.11	10.04	8.51	8.51	7.44	
Nd (ppm)	29.4	37.8	34.2	132.3	532.8	50.9	37.0	40.0	33.9	34.3	29.2	
Sm (ppm)	5.38	7.90	6.33	28.15	119.05	10.17	7.27	7.92	7.68	6.90	5.69	
Eu (ppm)	1.09	1.63	1.36	5.99	25.30	2.16	1.59	1.75	1.61	1.43	1.13	
Gd (ppm)	5.17	7.88	6.14	30.09	125.43	10.05	7.50	8.73	7.68	6.76	5.17	
Tb (ppm)	0.81	1.20	0.98	4.29	18.42	1.50	1.10	1.29	1.15	0.98	0.79	
Dy (ppm)	5.21	7.11	6.18	23.98	99.79	8.85	6.66	7.71	7.07	6.34	5.00	
Ho (ppm)	1.12	1.57	1.33	4.62	19.69	1.85	1.41	1.66	1.40	1.18	0.95	
Er (ppm)	3.63	4.49	3.92	12.81	48.39	4.99	4.23	5.06	4.14	3.70	3.03	
Tm (ppm)	0.55	0.67	0.60	1.64	6.13	0.78	0.64	0.66	0.59	0.51	0.42	
Yb (ppm)	3.77	4.30	4.01	9.10	32.48	4.66	3.90	4.44	3.73	3.25	2.90	
Lu (ppm)	0.57	0.65	0.63	1.29	4.34	0.72	0.60	0.67	0.57	0.51	0.44	
Mo (ppm)	224.0	126.4	68.8	96.2	/	57.7	262.3	204.9	244.7	223.9	193.3	
Cu (ppm)	207.1	176.2	189.7	188.0	/	151.2	116.8	100.9	110.0	99.7	98.1	
Zn (ppm)	1176	805	606	997	/	352	106	112	109	110	127	
Ni (ppm)	186.0	150.8	139.7	151.9	/	130.9	121.1	130.8	92.4	83.1	74.2	
Cd (ppm)	22.3	14.9	9.2	12.8	/	4.4	1.7	1.9	1.4	1.2	1.1	
TOC (%)	17.6	21.2	19.8	19.4	/	18.4	15.0	19.2	17.1	17.4	16.8	
S (%)	3.07	2.65	2.30	2.30	/	1.78	10.30	9.20	8.82	7.02	7.48	

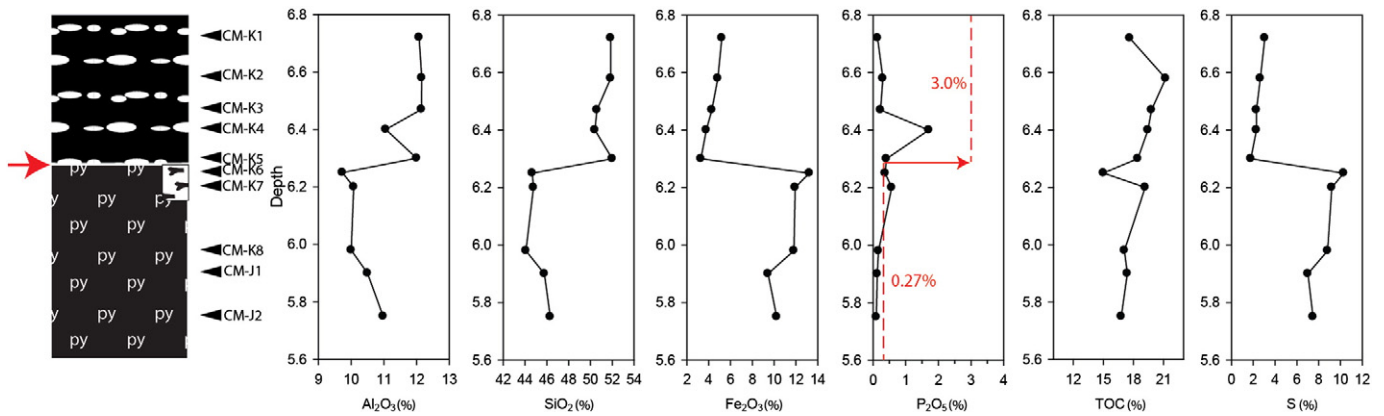


Fig. 8. Stratigraphic variation of major chemical constituents across the PBS to PhBS contact. A red arrow marks the erosion surface between the two units. Red dashed lines indicate the average P_2O_5 in the PBS and PhBS units.

interval (9.44–13.24 wt.%) and the PhBS interval (3.29–5.21 wt.%, Fig. 8).

Redox-sensitive trace elements (U, Mo, Co) were normalized to aluminum (Al) to examine their variability between the two shale intervals (Fig. 9). U, Mo, and Co show comparable trends with larger enrichments in the PBS unit (Fig. 8). Other trace elements, such as Cu, Ni, Cd, Zn, Cr, and V, show generally opposing trends with higher abundances in the PhBS interval (Fig. 9). The concentrations of rare earth elements have been normalized to PAAS. Samples from the background black shale matrix of both intervals show largely flat patterns with slightly negative Ce anomalies (Fig. 10A, B). Notable exceptions are samples CM-K4 (contains silty phosphatic bands) and CM-4b

(phosbioclast layer) with stronger phosphate enrichment and more pronounced negative Ce anomalies (Fig. 10B, C). Stratigraphic variability of carbon (C) and sulfur (S) is shown in Fig. 8. Total organic carbon (TOC) increases gradually from the PBS unit to the PhBS unit, ranging from 15.00 to 21.22 wt.% (Fig. 8). Sulfur distribution very closely matches the variability of iron (Fig. 8).

4.3. SEM observation in the PhBS unit

Significant numbers of phosphatic particles in the PhBS unit show evidence of dissolution. Dissolution is manifested in two ways: (1) as embedded pyrite crystals in the surface of phosphatic fossils (Fig. 11A,

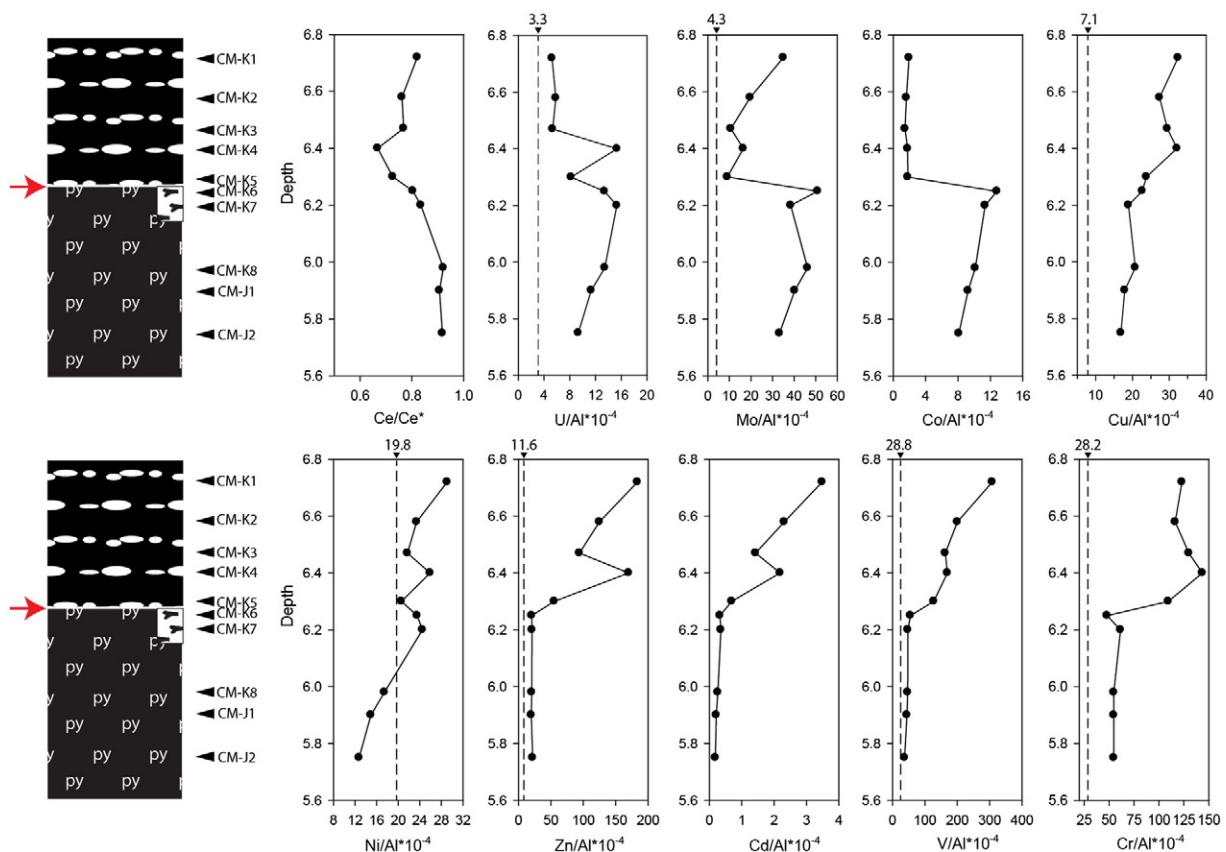


Fig. 9. Stratigraphic variation of Al-normalized trace element concentrations in the PBS and PhBS intervals. Red arrows mark the erosion surface between the two units. Dashed lines indicate Al-normalized enrichment of some trace elements as observed in the Black Sea (Calvert and Pedersen, 1993).

B, C) and (2) corrosion of the structure of phosphatic fragments (Fig. 11D, E, F). Under the optical microscope, many black pyrite spots (transmitted light) are on the surface of brachiopod, fish bone, and conodont fragments, giving the impression that pyrite crystals “grew” on the surface of fossil debris (Fig. 11A). When observed under the SEM, however, these euhedral pyrite crystals were embedded in the surface, indicating a replaceable relationship (Fig. 11B, C). Phosphate dissolution may be related to early diagenetic pyrite formation (see Discussion). Most pieces of phosphatic brachiopod debris show primary and secondary layers (e.g., Holmer, 1989). Primary layers consist of structureless apatite, whereas secondary layers show a partially dissolved structure of criss-crossing baculae (e.g., Holmer, 1989). Additionally, conodonts and fishbone debris may show dissolution along fractures and holes. Some partially dissolved fragments are surrounded by an overgrowth of structureless cryptocrystalline apatite (CCP) (Fig. 11J, K). Agglomerates of cryptocrystalline apatite can show deformation by compaction (Fig. 11L).

When examined with scanned cathodoluminescence, phosphatic fossils, cryptocrystalline apatite, and phosphate nodules show varying degrees of CL intensities (Fig. 12). Most phosphatic fossil debris is characterized by light gray to light blue CL. Overgrowth cryptocrystalline apatite shows a shift to a more bluish and intense CL response (Fig. 12A, B). Some agglomerates of cryptocrystalline apatite show a sky blue CL that is more intensive than overgrowth cryptocrystalline apatite (Fig. 12C, D). Apatite within phosphate nodules shows deepest blue color (Fig. 12E, F).

Besides of agglomerates of cryptocrystalline apatite, we also observed clusters of spherical apatite particles in the PhBS unit (Fig. 13) that morphologically resemble possible fossilized bacteria as observed in the Paleocene phosphorites from Ouled Abdoun (Cosmidis et al., 2013). These spherical objects show a narrow size distribution (1–3 μm) (Fig. 13A) and a multi-layered concentric structure (Fig. 13B, C, D). They are constructed with a bright and thick outer layer, a complete or incomplete bright inner apatite filling, and an intermediate low-density ring. Following Cosmidis et al. (2013) these are referred to as the outer precipitate, the inner precipitate, and the crown respectively (Fig. 13D, E, F). The crown consists of a dark matrix with embedded elongate apatite crystals. However, other clusters of spherical apatite particles are deformed. These deformed objects also show a narrow size distribution but lack a multi-layered concentric structure (Fig. 13G, H, I). Another potential microbial related feature is the occurrence of apatite grains within organic matter. These are distributed at variable density within organic matter (kerogen) (Fig. 14A, B). These crystals may show irregular as well as rounded to cylindrical shapes.

In phosphate nodules of the PhBS unit, the phosphatic matrix consists of “cloudy mottled” phosphate cements which show an internal radial texture at higher magnifications (Fig. 15A). Interstitial voids and pores are infilled by calcite cements (Fig. 15B). Two main kinds of *Tasmanites* cyst associated mineralization were observed: calcitic phosphatic *Tasmanites* cyst (CPT) (Fig. 16) and phosphatic *Tasmanites* cysts (PT) (Fig. 17). Most of CPT are filled with apatite, calcite, framboidal pyrite, marcasite and organic material. Some of pyrite framboids are at various stages of degradation (Fig. 16E). Organic walls of CPT are usually degraded, either fragmented or shrunk (Fig. 16A, D, F, G). PT are composed of apatite, framboidal pyrite, coarser pyrite cement, marcasite and organic material (Fig. 17). The main difference to CPT is that it lacks calcite. Unlike CPT, organic walls of PT are largely complete or just slightly shrunk (Fig. 17A, D, E). Some partially dissolved apatite grains also occur within areas of dominant calcite cement (Fig. 17E, G), whereas scattered residual apatite within calcite cement indicates calcite replacing apatite, rather than a sequence of events where dissolution created a void that was later on infilled with calcite (Fig. 17F).

The phosphatic shales described here have lateral equivalents in the New Albany Shale (upper portion of Clegg Creek Member) of Indiana and Kentucky and the Cleveland Shale of Kentucky and Ohio (Schieber

and Lazar, 2004; Lazar, 2007), and these shales and their phosphate nodules are texturally identical to those described here (Fig. 18). These nodules are also reworked (Fig. 18A), and their phosphatic matrix is the same as observed in the Chattanooga Shale (Fig. 18B, C). Relicts of phosphatic fossils, such as brachiopods, conodonts, and fish bones occur within nodules (Fig. 18D, E, F), as well as brownish round or irregular lumpy “grains” (Fig. 18F) which are phosphate cemented *Tasmanites* cysts and radial phosphate cements (Fig. 18G).

5. Discussion

5.1. Phosphatic layer: distribution and accumulation

Phosphatic fossil debris is a main source of phosphate in the two shale units in question, and its abundance and distribution should mirror the differences in P content and the potential for P-nodule formation. As outlined above, the background black shale of the PhBS interval shows a fourfold increase in phosphatic particles when compared to the PBS interval, and in reworked silty layers we see an order of magnitude increase of phosphatic particles as we go from PBS

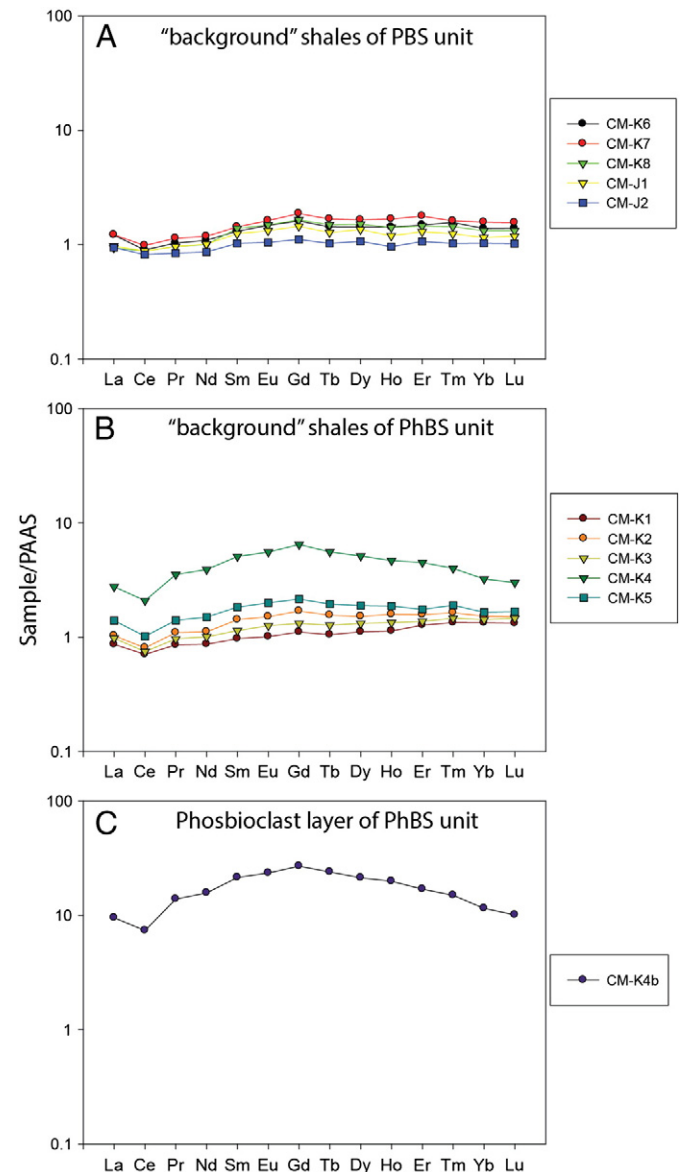


Fig. 10. PAAS-normalized REE patterns of samples in the PBS and PhBS units of the Chattanooga Shale, Chestnut Mound, Tennessee.

to PhBS (Fig. 5C, F, I). These differences, as well as the presence of reworked lags with even larger abundances of phosphatic debris suggest that phosphate enrichment in the PhBS is due to a combination of generally smaller sedimentation rates for the background sediment, as well as more frequent reworking and winnowing of the sediment once it had been deposited.

Sedimentation rate figures prominently to explain high P-enrichment in ocean sediments (Ingall and Cappellen, 1990; Follmi, 1996; Filippelli, 1997; Baturin, 1999; Dornbos, 2011). When combined with high primary productivity that can deliver large amounts of organic material to the seabed, low sedimentation rates result in organic enrichment of surface sediments (Follmi, 1996; Baturin, 1999; Dornbos, 2011). Decay of organic matter releases phosphate to pore waters, and once supersaturation is reached precipitation of hydroxylapatite occurs in pore spaces (Baturin, 1999). The average TOC in the PhBS unit (19.3 wt.%) is relatively higher

than in the PBS unit (17.1 wt.%) (Fig. 8; Table 1), indicating that decay of organic matter is a possible source of diagenetic P. Fragments of phosphatic fossils, on the other, differ systematically between the two units and suggest that strongly reduced net sedimentation rates in the PhBS interval can explain P enrichment. High sedimentation rates would also dilute the concentration of biogenic P-debris. Because the background shale of the PhBS unit is much more enriched in P-debris (37–88 particles per cm²) (Figs. 5I, 6D, H) than the black shale matrix of the PBS unit (8–16 particles per cm²) (Figs. 5C, F, 6A), is therefore an indication that overall sedimentation rates for the PhBS unit were lower than those for the PBS unit.

A second dimension of P-enrichment that we observe is reworking and winnowing of the seabed by bottom currents. These currents are probably due to large scale basin circulation, as well as wave interaction with the seabed. Mechanical remobilization, transport, and redeposition

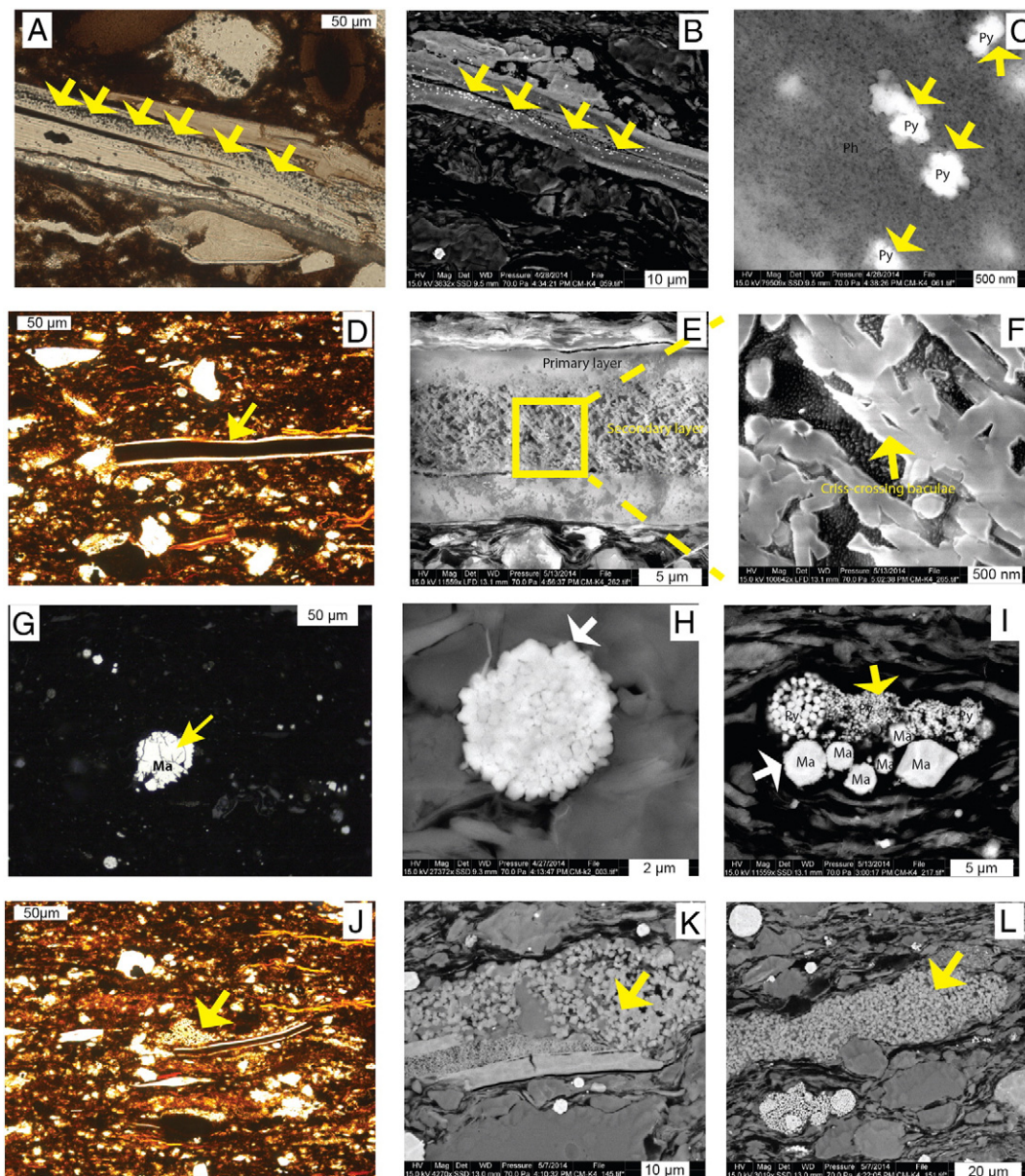


Fig. 11. (A) Photomicrograph of *Lingula* shell with embedded pyrite crystals (yellow arrows). (B) BSE image of partly pyritized *Lingula* shell. (C) Close-up image of pyrite crystals (yellow arrows), pyrite crystals replace the shell matrix. (D) Micrograph of shale with *Lingula* shell in center. (E) and (F) are secondary electron (SEM) close-up images that show the secondary layer in the *Lingula* shell. Notice criss-crossing baculae in the secondary layer. (G) Micrograph of shale with marcasite in the center. Notice anisotropic feature of marcasite (yellow arrow). (H) BSE image of a pyrite framboid with an overgrowth marcasite rim pointed out by a white arrow. (I) BSE image of framboidal pyrite and marcasite. Degraded pyrite framboids pointed out by a yellow arrow. (J) Micrograph of partially dissolved brachiopod fragments surrounded by overgrowth cryptocrystalline apatite (yellow arrow). (K) BSE image of partially dissolved brachiopod fragments overgrown by secondary cryptocrystalline apatite (yellow arrow). (L) Agglomerate of secondary reprecipitated cryptocrystalline apatite (yellow arrow).

of P-particles, in combination with repeated dissolution and reprecipitation of P, further concentrates P, (Follmi, 1996; Trappe, 1998; Baturin, 1999; Dornbos et al., 2006; Dornbos, 2011), a process that has also been termed “Baturin cycles”. Acting over multiple cycles of reworking, “Baturin cycles” cause significant stratiform concentrations of phosphate. (Follmi, 1996; Dornbos et al., 2006). With regard to abundance, the largest P-contents in the PhBS are observed in P-concretions, followed by phosbioclast layers, silty phosphatic bands, silty laminae or ripples and background shale (Figs. 5I, 6C, E, F). In the PBS unit, in contrast, above background P-values are only observed in association with bottom current produced silty laminae or ripples (Figs. 5F, 6B). This difference demonstrates that reworking and winnowing events are the most significant mechanical process of

concentrating phosphatic fragments in the PhBS unit. The comparatively high density of phosphatic debris (2.9 g/cm^3 ; (Follmi, 1996)) further enhances selective sediment transport during winnowing, selectively removing clays, particulate organic matter, and fine silt, and leaving behind larger and heavier P-debris (Trappe, 1998). Whereas the P-nodules represent the end-point of physico-chemical P-concentration, the other non-concretionary types of P-enrichment, normal and inversely graded phosbioclast layers and silty phosphatic bands, provide information about seafloor processing of the initial sediment (Figs. 4B, 5G, H, 19). Phosbioclast layers above jagged erosion surfaces indicate substantial erosive energy and removal of several decimeters of substrate (Schieber, 1998). Normal graded phosbioclast layers are considered the result of reworking/winnowing events that waned gradually

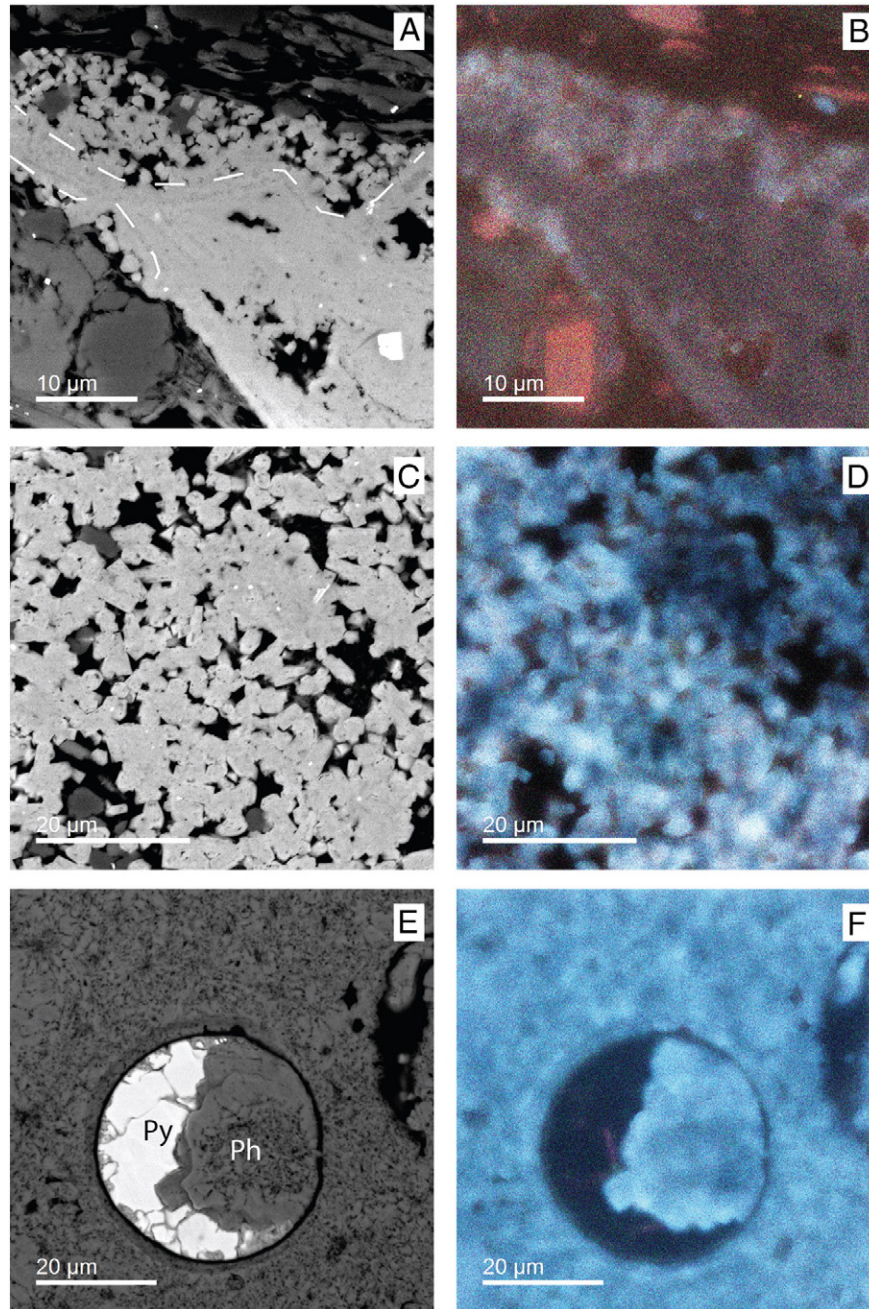


Fig. 12. (A) BSE image of phosphatic fossil debris with overgrowth cryptocrystalline apatite crystals in the PhBS unit. The edges of phosphatic fossils are marked by dashed white lines. (B) Cathodoluminescence (SEM-CL) image of phosphatic fossil debris with overgrowth cryptocrystalline apatite crystals. The secondary cryptocrystalline apatite shows intense blue CL. (C) BSE image of cryptocrystalline apatite agglomerates in the PhBS unit. (D) CL image of cryptocrystalline apatite agglomerates in the PhBS unit. Notice the sky blue CL of these apatite crystals. (E) BSE image of phosphate cements in a phosphate nodule. (F) CL image of phosphate cements in a phosphate nodules. Note intensely blue CL. Ph = phosphate, Py = pyrite.

(Fig. 19C), whereas silty phosphatic bands are thought to be caused by longer term action of moderate current and wave action (Fig. 19D). In contrast, inverse graded phosbioclast layers are thought to reflect gradual increase in bottom energy from moderate to high (Fig. 19B). Cumulatively, our observations indicate that the abundant of P-debris serves as a proxy for the average energy level at the seabed. Stratigraphic variability of P-enrichment from cm to cm indicates fluctuating intensity of bottom current activity and may even reflect high order sea level fluctuations.

In addition, the distribution of organic particles also suggests much lower sedimentation rate and enhanced reworking of the seabed during deposition of the PhBS interval. Given that the inertinite that has been observed in these shales (Fig. 7) is probably land-derived fossil charcoal (Rimmer et al., 2004), the much higher abundance of inertinite in the PhBS unit (5.6%; Fig. 7B) relative to the PBS unit (1%; Fig. 7A) is consistent with concentration of inertinite in the PhBS via combination of low sedimentation rate and reworking & winnowing.

5.2. Phosphate remineralization: dissolution and reprecipitation

There are four possible sources of dissolved phosphate in sediments: microbial breakdown of labile organic matter (e.g., Ingall and Cappellen, 1990), phosphate desorption from iron and manganese oxyhydroxides,

dissolution of phosphatic fossil debris, and direct precipitation of sea-water phosphate at the sediment–water interface (e.g., Follmi, 1996). Calcium phosphate can dissolve under acidic or near neutral conditions (e.g., Christoffersen, 1981; Dorozhkin, 2002; Dorozhkin, 2012) and precipitate under neutral to weakly alkaline conditions (Lucas and Prevot, 1991; Briggs and Wilby, 1996; Trappe, 1998). The dissolution features observed in the PhBS unit, replacement of phosphate by pyrite and partial dissolution of phosphatic fossil debris (Fig. 11A, B, C, D, E, F) reflect two different aspects of dissolution. Pyritization implies dissolution contemporaneous with pyrite precipitation, suggests a role of bacterial sulfate reduction in the process (e.g., Raiswell, 1997). Partial dissolution of phosphate fossils, especially brachiopod shells (Fig. 11E, F), in the PhSB unit suggests significant lowering of pore water pH values. Phosphatic brachiopods, such as *Lingula*, have a shell with primary and secondary layers, and the latter have been made visible by acid etching in prior studies. Etching brings out a network of criss-crossing baculae in the secondary layer (Holmer, 1989; Nemliher et al., 2004; Puurař and Lang, 2013) that closely resembles the secondary layer structure seen in this study (Fig. 11E, F). This suggests that the observed structures (Fig. 11E, F) record etching by intermittently acidic pore waters. Dissolved “fractures” or “holes” in other phosphatic fossil debris (conodonts, fishbone) provide further support for intermittently acidic pore waters.

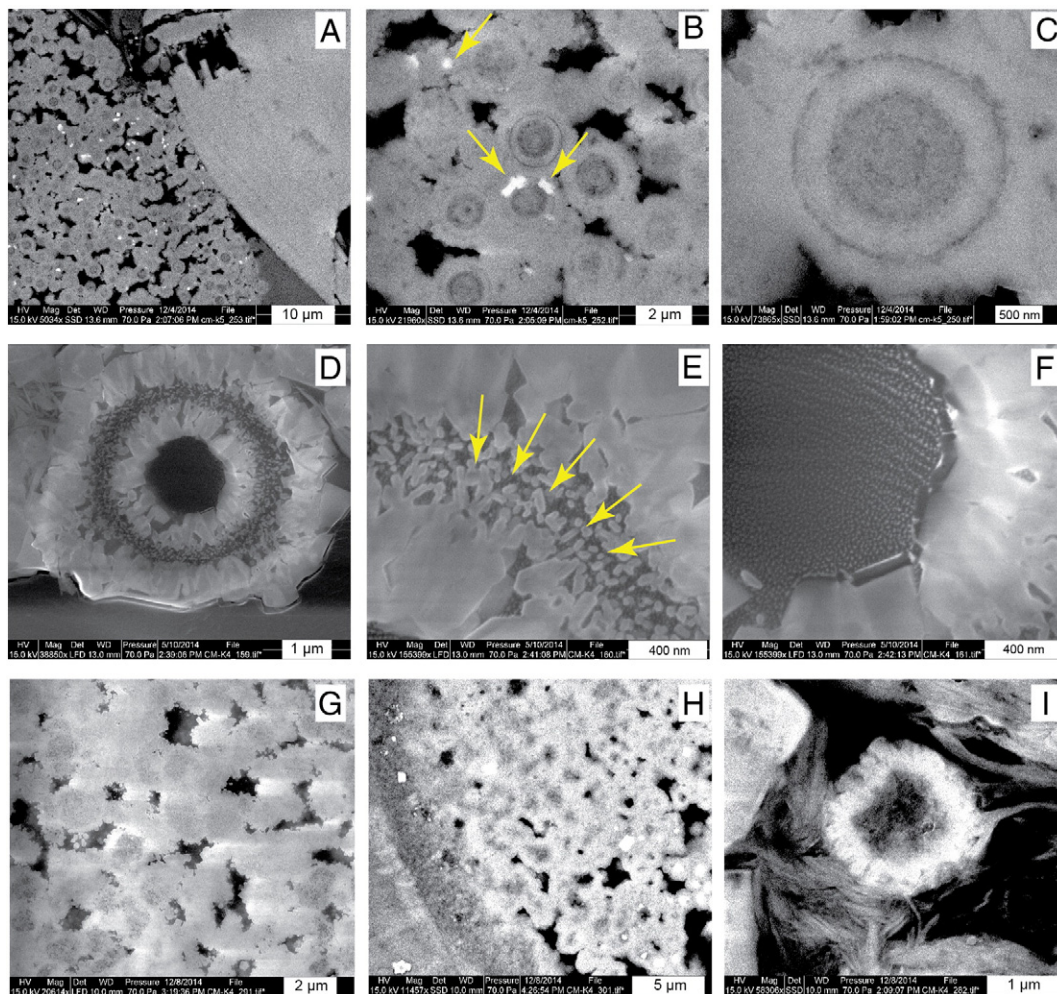


Fig. 13. (A) BSE image of agglomerate of spherical apatite particles. Note narrow size distribution of spherical objects. Phosphatic fragment in the top right corner is a fish bone. (B) Close-up BSE image of spherical objects. Notice the pyrite crystals (yellow arrows) that are embedded within these spherical objects. (C) Nanometer-scale BSE image of individual spherical apatite particle. Notice multi-layered concentric structure. (D) SEM image of individual spherical apatite objects. Notice the dark crown is surrounded by a bright outer precipitate and inner precipitate. (E) Close-up of the crown that is composed of needle-shaped crystals (yellow arrows). (F) Close-up of incomplete inner precipitate. Notice organic matter inside the cell. (G) BSE image of agglomerate of deformed spherical apatite objects. (H) BSE image of secondary apatite objects inside a fish bone. (I) BSE image of a deformed spherical object.

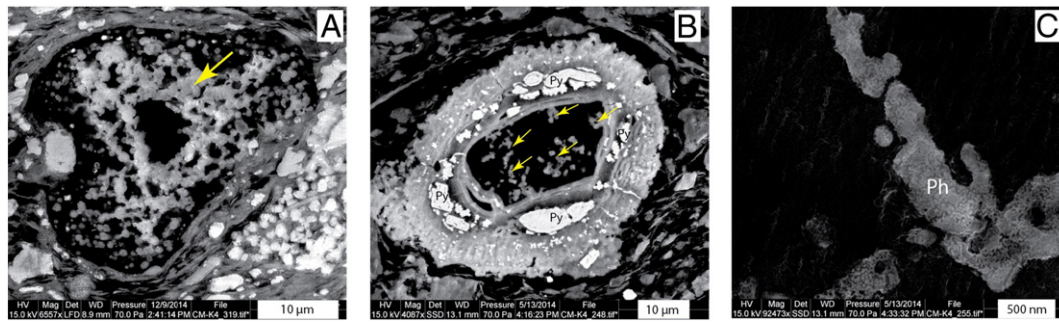
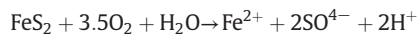


Fig. 14. (A) A cluster of apatite crystals (yellow arrow) mingled with organic matter. (B) Some scattered apatite crystals (yellow arrow) suspended in organic matter inside a fish bone. (C) Close-up BSE image of phosphate precipitate from (B). Ph = phosphate, Py = pyrite.

A possible driver for lowering pore water pH is the oxidation of early diagenetic pyrite, which promotes the subsequent formation of marcasite (Schieber, 2007; Schieber, 2011) and is illustrated with the following equation:



This reaction is consistent with observations of carbonate dissolution due to iron-sulfide oxidation in modern muds (Reaves, 1986) and was further confirmed by the recognition of marcasite formation from iron sulfides in marine lags and black shales (Schieber and Riciputi, 2005; Schieber, 2007; Schieber, 2011). The common observation of marcasite in the PhBS unit, associated with degradation of pyrite framboids (Fig. 11G, H, I) is consistent with the assumption of intermittently lower pH levels and phosphate dissolution.

The sharp drop of Fe content when going from the PBS unit to the PhBS unit (Fig. 8) provides another piece of the puzzle in explaining the distinctions between the two shale units. Previous studies of the marine iron cycle have shown that significant amounts of iron are transported from the continental shelf to the deeper ocean (de Baar and de Jong, 2001; Poulton and Raiswell, 2002; Aumont and Bopp, 2006; Raiswell et al., 2006; Moore and Braucher, 2008; Lancelot et al., 2009; Tagliabue et al., 2009; Raiswell, 2011; Taylor and Konhauser, 2011), a process described as the “benthic iron shuttle”. In conditions where sulfate reduction is suppressed, Fe (II) in the pore waters of shallow-shelf sediments, formed by bacterial iron reduction (Taylor and Macquaker, 2011), is reoxidized during sediment reworking and resuspension events and generates fine-grained iron oxides (nanoparticles and aqueous species) that are transported by current into deeper water (Raiswell, 2011; Taylor and Konhauser, 2011). The drop of iron contents in the PhBS unit suggests that episodic shelf reworking exposed Fe-rich pore waters to oxidation and led to formation of fine grained solid iron phases (oxides and oxyhydroxides). Although some

of these fine grained iron solids may be redeposited and fixed again as pyrite, repeated cycles of reduction, resuspension and re-oxidation are likely to allow a portion of them to be carried by currents into deeper water (Lyons and Severmann, 2006). We propose therefore that iron depletion in the PhBS is due to the operation of the (reworking supported) benthic iron shuttle, and that significantly lesser amounts of reworking in the PBS exposed less pyrite to reoxidation and potential removal as iron oxide solids.

The observed Ce anomalies also suggest that deposition of the PhBS unit occurred under more oxygenated and probably shallower conditions (Figs. 9, 10). The negative Ce anomaly is related to the oxidation of Ce (III) to immobile Ce (IV) (Sholkovitz et al., 1994), and therefore has been used as indicator of depositional environment of fine-grained sediments (Murray et al., 1991), and to trace redox conditions (Elderfield and Greaves, 1982; Wilde et al., 1996). Negative Ce anomalies are small in both shale units, but better developed in the PhBS unit (avg. = 0.73; Fig. 9), suggestive of better bottom water oxygenation in the PhBS unit.

Trace elements have also been widely used as indicators of paleo-redox conditions (e.g., Berner, 1980; Huerta-Diaz and Morse, 1990; Emerson and Huested, 1991; Calvert and Pedersen, 1993; Piper, 1994; Crusius et al., 1996; Helz et al., 1996; Sageman et al., 2003; Algeo and Maynard, 2004; Tribouillard et al., 2006). Enrichments of U, Mo, and Co are generally higher in the PBS unit than in the PhBS unit, coincident with smaller Ce anomalies. Enrichment of U in phosphate (Jarvis, 1995; Trappe, 1998) explains the abnormal U values of phosphoclast sample CM-K4. Other trace elements (V, Cu, Ni, Zn, Cr, Cd), however, show inverse trends of enrichment, meaning that they are more enriched in the PhBS unit. For the PhBS unit, the abundances of U, Mo, and Co would imply a more oxygenated setting than unit PBS, whereas V, Cu, Ni, Zn, Cr, and Cd trends would suggest that it was deposited in a more oxygen restricted setting. This seeming contradiction (Fig. 9) could be due to a change in organic matter composition.

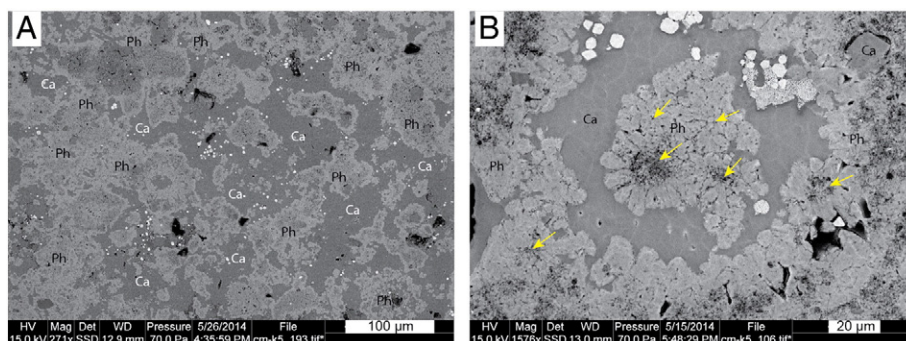


Fig. 15. (A) BSE image of background matrix within a phosphate nodule from sample CM-K5. Notice the “cloudy-mottled” phosphate cements (light gray is phosphate, dark gray is calcite). (B) Close-up of “cloudy-mottled” phosphate cements. Notice the internal radial texture within cements (yellow arrows). Ca = Calcite, Ph = phosphate.

In previous studies it was noticed that some trace elements are prefer to be concentrated in specific organic matter types (e.g., Pareek and Bardhan, 1985; Lyons et al., 1990; Palmer and Lyons, 1990; Robl et al., 1992; Spears and Zheng, 1999; Wang et al., 2003). The PhBS unit contains more alginite and inertinite than the PBS unit, and this difference could potentially explain the difference in trace element incorporation (Fig. 7). This issue probably needs further analysis for the rocks at hand, but nonetheless serves as a reminder that one needs to proceed with caution when using trace elements as indicators of redox condition.

In the PhBS unit, partial dissolution of phosphatic fossil debris and secondary overgrowths of cryptocrystalline apatite (Fig. 11J, K) attest

through their spatial relationships to multiple cycles of dissolution and reprecipitation. The concept that cryptocrystalline apatite is the result of reprecipitation of previously dissolved is consistent with the previously discussed evidence for pH lowering that forces dissolution of phosphate and raises the dissolved P-concentration in the pore waters. Because the remaining (after dissolution) phosphatic grains serve as a crystallization seed, it will be there were overgrowth will occur once supersaturation is reached, acidity generating reactions (e.g., Schieber, 2007) cease, and pH levels increase (Lucas and Prevot, 1991; Briggs and Wilby, 1996; Trappe, 1998). In thin section, cryptocrystalline apatite that does not appear overgrowing fossil fragments may either represent a surface that did not intersect and underlying fossil fragment,

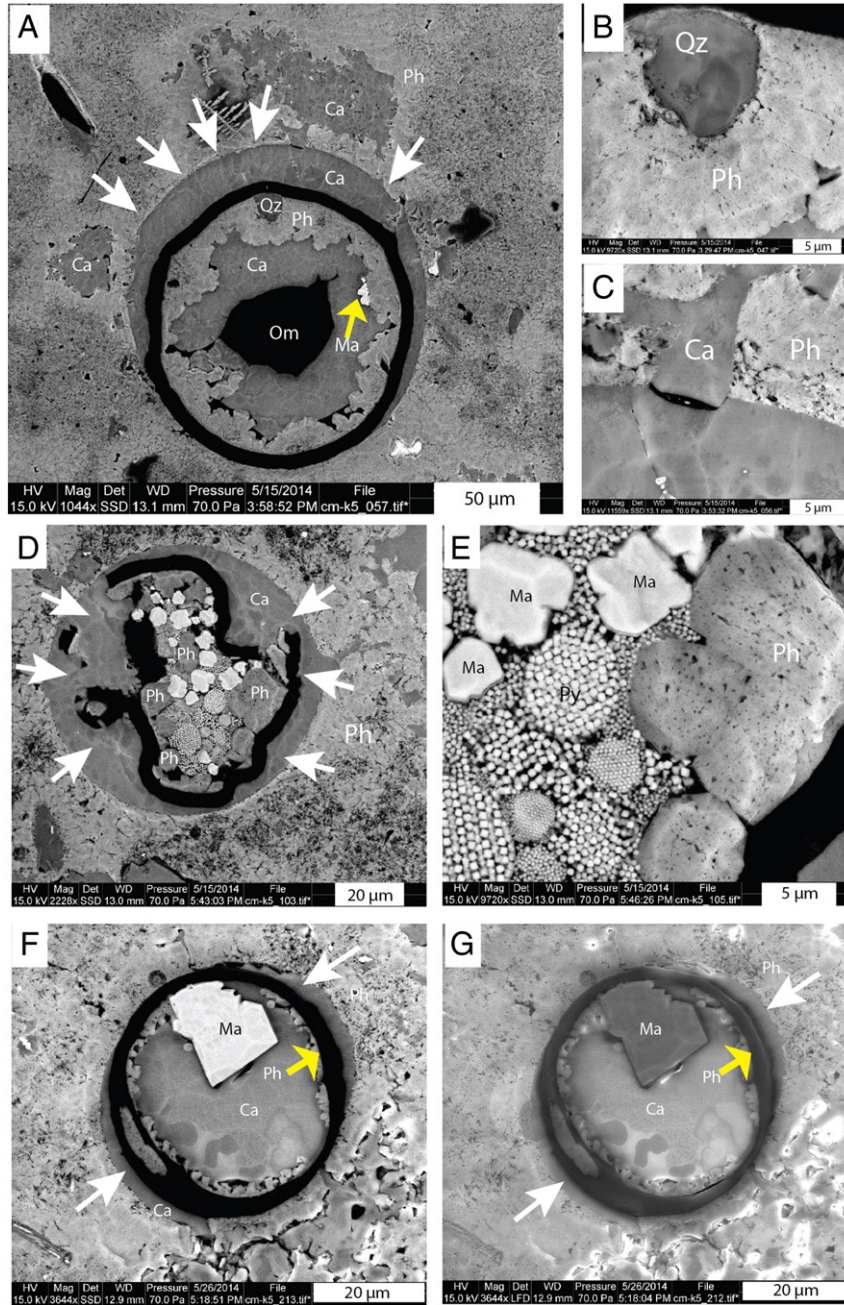


Fig. 16. (A) BSE image of *Tasmanites* cyst in phosphatic matrix, filled with organic matter, calcite, apatite, and quartz. Notice the shrunken wall of *Tasmanites* cyst (white arrows). (B) Close-up of quartz along the wall of cyst. Quartz (Qz) grew prior to apatite. (C) Close-up of void filling calcite. Void caused by shrinkage of cyst wall. Cross-cutting relationships between calcite and apatite suggest replacement of apatite by calcite. (D) Shrunken *Tasmanites* cyst associated with apatite, pyrite, marcasite, and calcite. Notice the collapsed wall of the cyst (white arrows). (E) Close-up of contact relationships among pyrite, marcasite and apatite, notice the partial degradation of pyrite framboids. BSE image (F) and SEM image (G) of calcite cemented *Tasmanites* cyst in phosphatic matrix, filled with calcite, marcasite, and apatite. Notice the shrinkage of cyst wall (white arrows). Ca = Calcite, Ph = phosphate, Py = pyrite, Qz = Quartz, Ma = marcasite, Om = Organic matter.

or it precipitated in available pore spaces once all available fossil surfaces were covered (Fig. 11L).

The observed REE patterns (Fig. 10) are also consistent with the former action of dissolution and reprecipitation of fossil apatite in the PhBS unit (Fig. 10). Leaching experiments show that preferential dissolution of apatite under acidic pH leads to MREE enrichment in water column (Hannigan and Sholkovitz, 2001), and that precipitation of apatite from seawater results in the preferential removal of dissolved MREE from pore waters and the formation of MREE-enriched apatite (Byrne et al., 1996). Thus, through multiple cycles of dissolution and reprecipitation significant enrichment of MREE can occur in phosphate-rich layers, such as in samples CM-K4a and CM-K4b (Fig. 10).

Scanned cathodoluminescence imaging (SEM-CL) further reinforces above view of repeated dissolution–precipitation cycles of cryptocrystalline apatite (Fig. 12). CL-microscopy and -spectroscopy are a powerful tool to confirm the structural incorporation of activator elements and supplement conventional trace element analysis (Richter et al., 2003). Blue CL is intrinsic for apatite and fossil francolite (Habermann et al., 2000) due to activation by trace quantities of REE ions (Ce^{3+} , Eu^{2+} , Sm^{3+} , Dy^{3+} , and Nd^{3+}) (Kempe and Götze, 2002). Thus, there is a positive correlation between CL intensities and REE enrichments (Habermann et al., 2000). Based on these studies, the brighter blue colors of overgrowth apatite (Fig. 12) indicate REE enrichment due to dissolution–precipitation cycles (Byrne et al., 1996;

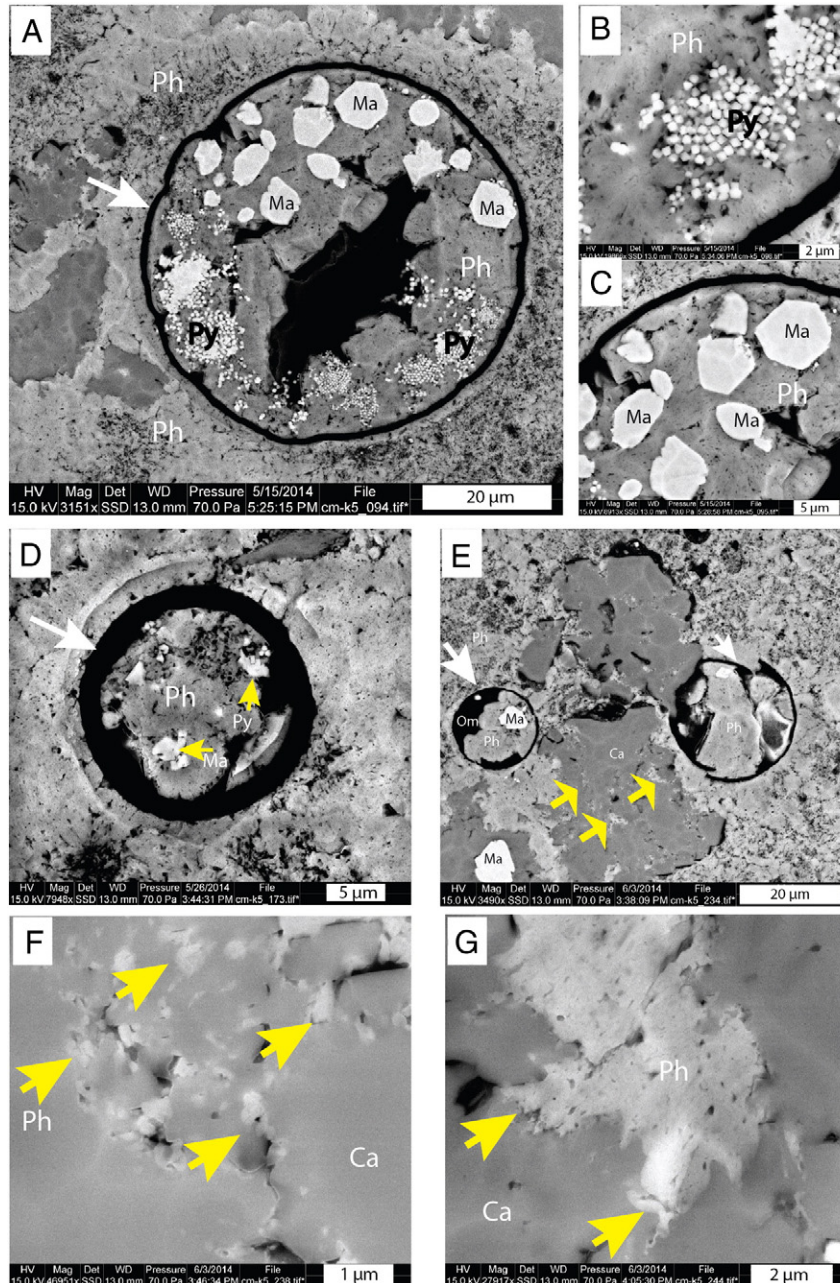


Fig. 17. (A) BSE image of *Tasmanites* cyst in phosphatic matrix, filled with organic matter, apatite, marcasite, and pyrite. Shrinkage of *Tasmanites* cyst (white arrows) allowed infill precipitation of apatite in the gap. (B) Close-up of partially degraded pyrite framboids in the interior of cyst. Close-up of euhedral marcasite in the cyst. (D) *Tasmanites* cyst in phosphatic matrix, filled with apatite, pyrite, and marcasite. (E) *Tasmanites* cysts in phosphatic matrix that has been partially replaced by calcite. Calcite occupies irregular domains within the nodule. Yellow arrows mark residual phosphate within calcite. (F) Close-up of calcite that shows scattered residual apatite within calcite cement (Yellow arrows). This relationship suggests calcite replacing apatite, rather than a sequence of events where dissolution created a void that was later on infilled with calcite. (G) Close-up of contact relationship between apatite and calcite. Notice the corroded edge of the apatite grain (Yellow arrows). Ca = Calcite, Ph = phosphate, Py = pyrite, Qz = Quartz, Ma = marcasite, Om = Organic matter.

Hannigan and Sholkovitz, 2001), and the speckled pattern of various degrees of blue CL intensities in the overgrowth (Fig. 12B, D, F) imply multiple and successive episodes of dissolution–reprecipitation and REE enrichment (increasing intensity of blue CL) and different stages of reprecipitation processes. The most intensive blue CL is observed in the apatite of phosphate nodules, which

shows that phosphate nodules represent the final stage of many preceding dissolution–reprecipitation cycles (Fig. 12E, F). The petrographic, SEM-CL, and geochemical observations made on the PhBS unit all converge to support an interpretation that calls on P-enrichment via multiple episodes of mechanical reworking coupled with dissolution–reprecipitation processes.

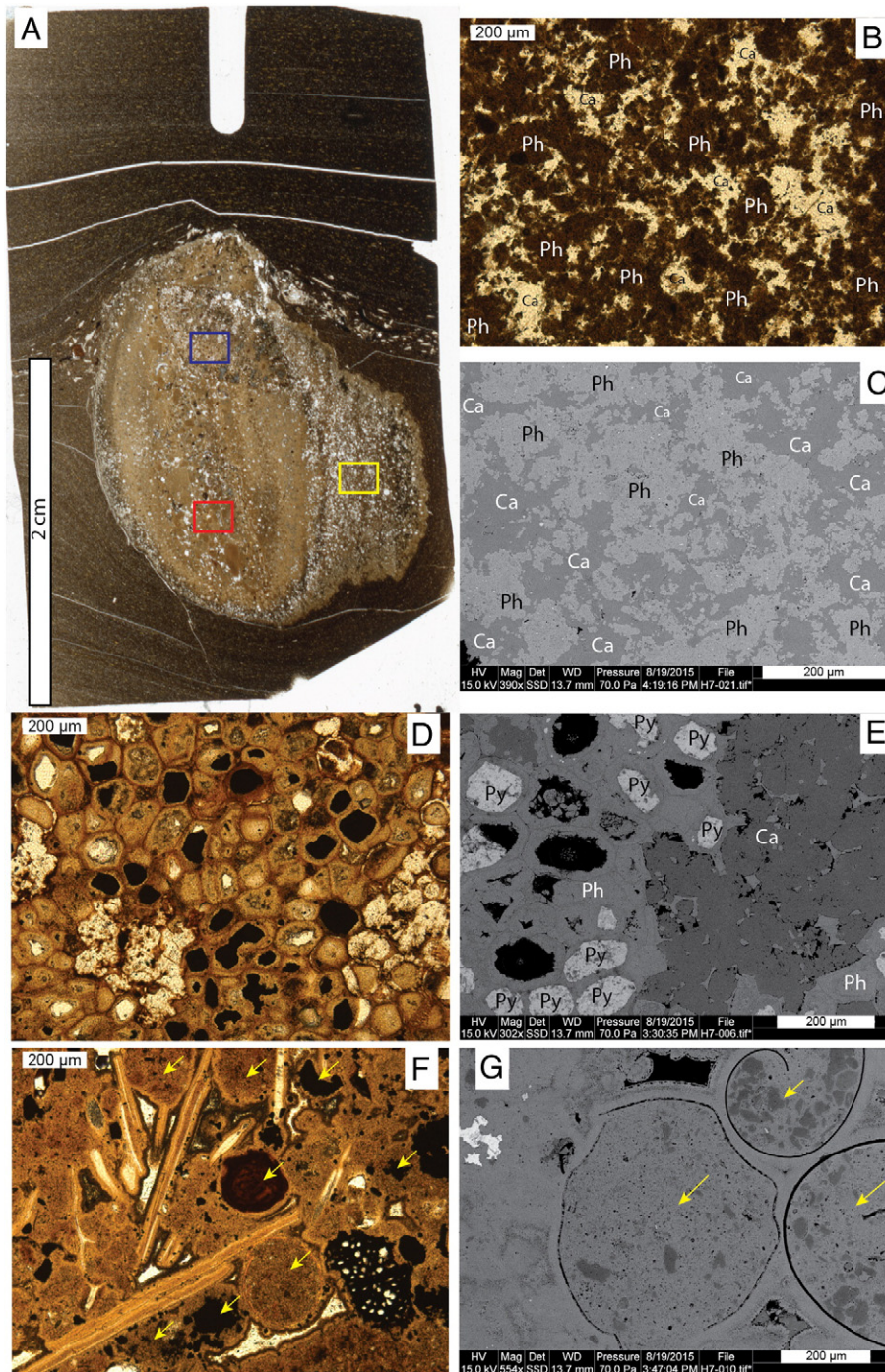


Fig. 18. (A) Photomicrograph of a phosphate nodule sample from the New Albany Shale (upper portion of Clegg Creek Member), Indiana. Internal layering indicates that the nodule is rotated by 90°, most likely a result of intermittent erosion, reworking, and transport. Colored rectangles are locations of close-up microscopic images, transmitted light and BSE. (B) and (C) are from the yellow rectangle and show the cloudy-mottled texture of the nodule matrix. (B) is transmitted light, and (C) is a BSE image. (D) and (E) are from the blue rectangle area and show details from fish bone fragments. (D) shows the sponge-like structure of fish bone material (transmitted light), and (E) shows partial replacement of fishbone by pyrite and calcite (BSE image). (F) and (G) show close-up images of the nodule fabric from the red rectangle area. (F) shows phosphatic fossil debris surrounded by brownish rounded and lumpy masses of matrix phosphate (transmitted light). (G) shows phosphate filled *Tasmanites* cysts (yellow arrows) in a BSE image. Note that the organic walls of these cysts are not collapsed, indicating cementation near the sediment–water interface. Ca = Calcite, Ph = phosphate, Py = pyrite.

5.3. Other possible origins of phosphate

In modern ocean systems, upwelling of deep ocean waters is considered an important factor for formation of phosphate-rich sediments along continental margins (e.g., Kazakov, 1937; Burnett, 1977; Baturin, 1982), and this model has been used as an analog for some ancient sediments (e.g., McKelvey, 1959; Parrish, 1982; Kidder, 1985; Cook and O'Brien, 1990; Piper and Link, 2002). Upwelling currents are a phenomenon of the outer shelf to upper slope (Trappe, 1998), and therefore, many ancient phosphorites or phosphate-rich sediments that were deposited in shallow inner shelf and epicontinental settings are not readily explained with an upwelling model (Glenn et al., 1994). In the Devonian of the southern US, siliceous-cherty facies of the Upper Devonian Woodford Shale is considered deposited along the Devonian continental margin in upwelling setting (Parrish, 1982), with anomalously high silica due to upwelling-driven high radiolarian productivity. As one follows the Woodford Shale to the north, however, into the interior of the Devonian inland sea (Conant and Swanson, 1961) the siliceous facies fades out and it becomes a dominantly carbonaceous shale that shows no influence of upwelling (Erik and Bynum, 2014). A similar facies transition from Devonian continental margin to continental interior is also described for the Chattanooga Shale (Conant and Swanson, 1961), where, as one follows the Chattanooga Shale north

from Georgia and Alabama to Tennessee, siliceous-cherty facies occurs near the ancient Devonian margin and carbonaceous shales prevail in the continental interior. Our study area in Tennessee is located in a shallow epicontinental basin at least 500 km away from the Devonian continental margin (Schieber, 1998), and it is doubtful whether upwelling currents could have extended that far north in a shallow sea (Schieber, 1994a; Trappe, 1998). The fact that lateral equivalents of the phosphatic shales investigated here extend as far north as northern Ohio (the Cleveland Shale; Schieber and Lazar, 2004; Lazar, 2007), approximately 1000 km north of the continental margin, further suggests that P-supply via upwelling is not a viable mechanism for the phosphatic black shales that accumulated in the Devonian inland sea.

Phosphatic fecal pellets from zooplankton are observed within modern and ancient phosphate-rich sediments and are considered as a possible source of phosphate (Porter and Robbins, 1981; Kidder, 1985; Slatt and O'Brien, 2011). Some brownish round or lumpy "grains" are found within nodules in the PhBS unit and its equivalents in Indiana (Fig. 18F). Most of them, however, are phosphate filled Tasmanites cysts (Fig. 18F, G). Their largely uncollapsed nature suggests phosphate cementation in surficial sediments, comparable to silica and pyrite filled cysts in these same sediments (Schieber, 1996; Schieber et al., 2000; Schieber and Baird, 2001). In addition, no phosphatic pellets were found in the background shale matrix surrounding the nodules. Instead,

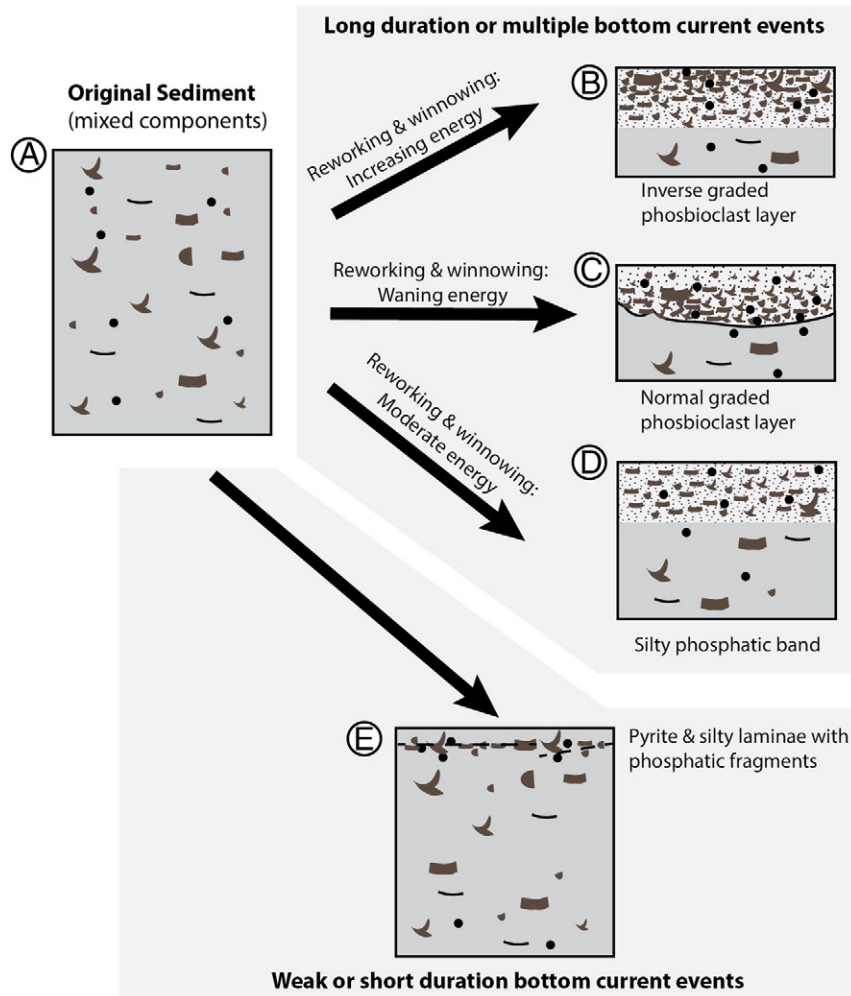


Fig. 19. Schematic model for concentration of phosphate in the PhBS unit. (A) Background black shale with low sedimentation rate in the PhBS unit. Brownish fragments stand for phosphatic particles. Black balls stand for pyritic particles. Black streaks represent organic matter. In the case of long duration or multiple bottom current reworking events, a large portion of the originally deposited mud has been eroded and removed. Normal graded phosbioclast layers are considered the result of reworking/winnowing events that waned gradually (C), inverse graded phosbioclast layers reflect gradual increase in bottom current energy (B). Silty phosphatic bands are results of longer term action of moderate energy current and wave action (D). In the case of short term bottom current events, only a small portion of the black shale matrix has been removed, and phosphatic particles are concentrated along pyritic-silty laminae or ripples (E).

phosphatic fossil debris is the predominant phosphatic component in the host sediment of the (Figs. 6, 18D, E, F). Its common incorporation into phosphate nodules (Fig. 18) strongly suggests that phosphatic fossil debris is the main source of phosphate in these shales.

Microorganisms, especially sulfur oxidizing bacteria, can play both a passive role and an active role in the precipitation or reprecipitation of phosphates. Cells of bacteria can for example serve as templates for the nucleation and growth of apatite in a phosphate oversaturated solutions (Sigel et al., 2008). On the other hand, bacterial phosphatases in the periplasm of sulfur bacteria actively liberate phosphate following the degradation of organic compounds (Hirschler et al., 1990; Blake et al., 1998). Such a mechanism operates in recent phosphorite forming environments (e.g., Schulz and Schulz, 2005; Arning et al., 2009). Via morphologic resemblance, micrometer-sized spherical, rod-shaped, or filamentous apatite bodies found in phosphatic sediments, have been linked to modern microbial cocci, bacilli, or filaments (e.g., Bailey et al., 2007; Bailey et al., 2013; Lepland et al., 2013). Most of the modern analogs were large sulfur bacteria. Nanometer-scale phosphatic fossils of bacteria have also been found recently (Cosmidis et al., 2013) and are supported by experiments of gram-negative bacteria (Benzerara et al., 2004). Some of the potential microbes in the PhBS (Fig. 13A, B, C, D, E, F) show morphologic resemblance to these nanometer-scale bacteria. A narrow size distribution of these objects (1–3 μm)

(Fig. 13A) future exclude possibility of abiotic chemical processes (Cosmidis et al., 2013). These clusters of particles show a sparse distribution, indicating microbial bacteria may not play significant role for reprecipitation of phosphate. Origin for other clusters of deformed phosphatic particles (without multi-layered concentric structure and crown feature) (Fig. 13G, H, I) is still questionable. The occurrence of apatite grains within organic matter (Fig. 14A, B, C) may imply microbial degradation of organic matter, which releases phosphate to pore waters and promotes reprecipitation of phosphate (Baturin, 1999).

5.4. Diagenesis in phosphate nodules

In the course of a lengthy history of phosphate diagenesis, not only did soluble phosphate re-precipitate as overgrowth cryptocrystalline apatite crystals, but it also filled in *Tasmanites* cysts that were part of the original sediment. Various combinations of apatite and calcite cements in association with *Tasmanites* cysts (CPT and PT) give additional information on diagenetic processes during formation of the nodules. The spatial relationships between apatite and calcite seen in Figs. 16 and 17 indicate that calcite precipitated later than apatite. Precipitation of apatite usually occurs in the surface sediment as it oscillates between the suboxic (e.g., Froelich et al., 1979; Krom and Berner, 1981) and to sulfate reduction zone (e.g., Raiswell, 1976; McArthur et al., 1980),

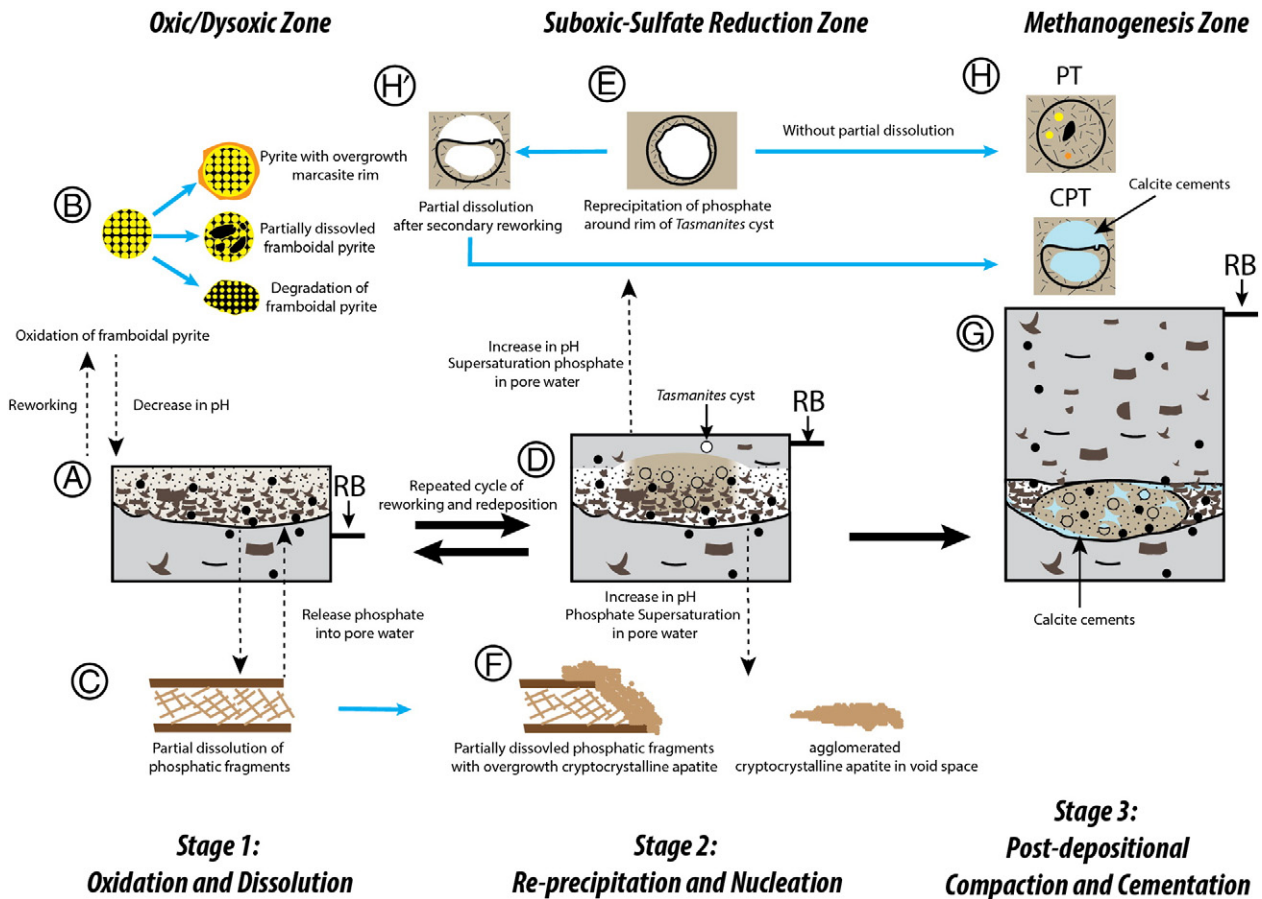


Fig. 20. Schematic model for the formation of phosphate nodules in the PhBS unit. (A) Severe long term reworking and erosion events lead to intermittent downward shift of the redox boundary (RB). The redox boundary (RB) is at the base of the erosion surface. This allows partial oxidation of pyrite particles (dissolution and degradation of framboidal pyrite) within the phosphatic intervals (B), causes a drop of pore water pH and enables marcasite formation, and also leads to partial dissolution of phosphatic fragments (C) and release of phosphate to pore waters. Dissolved phosphate in pore waters builds up to supersaturation levels, and gives rise to apatite precipitation when pore water acidity dissipates and pH rises again (D). Upward movement of the redox boundary due to continued accumulation of matrix moves phosphatic intervals into the suboxic/sulfate reduction zone. Both increasing pH and upward shift of redox boundary favor reprecipitation of phosphate, and result in overgrowth cryptocrystalline apatite around partially dissolved phosphatic fragments (F) and reprecipitation of phosphate along *Tasmanites* cyst (E). This cycle of reworking, dissolution and reprecipitation can be repeated multiple times. With deeper burial the sediment passes into the methanogenic zone and dissolution voids within phosphate nodules are cemented by calcite (G). Some *Tasmanites* cysts (H) are largely phosphatic cemented (PT), whereas in other places the phosphatic matrix has been partially dissolved (H') and has later been cemented by calcite (CPT). Large solid arrows indicate principal transformations. Blue solid arrows indicate characteristic changes among related components. Dashed arrows mark chemical or physical processes.

whereas calcite is likely to precipitate at somewhat greater burial depth where microbial methanogenesis occurs (e.g., Dix and Mullins, 1987; Morad and Alaasm, 1994). The pH levels needed for precipitation of apatite are around 7, levels at which calcium carbonate starts to dissolve (Lucas and Prevot, 1991; Briggs and Wilby, 1996; Trappe, 1998). At normal seawater pH conditions (~8 or slightly above) calcium carbonate is more stable than phosphate and thereby inhibits phosphate precipitation even though pore water is typically saturated with respect to phosphate (Dornbos, 2011). The observed textural relationships between apatite, pyrite, and calcite in nodules indicate that precipitation of apatite occurred first in the suboxic to sulfate reduction zone at shallow burial depth below the sea floor, followed by precipitation of secondary pyrite. Strong bottom currents eroded and winnowed sediment, as well as reworking and rotating phosphate nodules (Figs. 3C, 18A). This also forced a downward migration of the redox boundary in the sediment and caused formation of secondary marcasite. The acidity associated with the latter process (e.g., Schieber, 2007) also caused partial dissolution of phosphate particles and later reprecipitation of phosphate and further growth of phosphate nodules. Upon deeper burial, remaining pores within nodules were cemented by calcite as the sediment passed through the zone of methanogenesis (e.g., Figs. 16A, 17F, 20), and some phosphate was replaced by calcite (Fig. 17F).

6. Conclusions

As observed in this study, phosphogenesis in the upper Chattanooga Shale is to a large degree driven by coupling of mechanical reworking and dissolution–reprecipitation processes in surficial sediments. Although microbial mediation and colonies as well as other phosphate origins, such as upwelling and fecal pellets, can play an important role in primary phosphogenesis, they do not appear to have been a major factor. The high phosphate content in the PhBS appears to be a combination of smaller overall sedimentation rates, coupled with reworking/winnowing episodes that strongly concentrated phosphatic fossil debris. A hierarchy of mechanical phosphate enrichment was observed, going from phosphatic silty laminae, over phosbioclast layers, to pebble-size reworked nodules. Apatite dissolution and reprecipitation resulted from a complex interplay of chemical interactions between Fe (benthic iron shuttle), sulfate and sulfides (pyrite, marcasite), and was mediated by microbial consortia that occupied the sediment. High energy events and bottom currents were essential for phosphate enrichment, and the associated chemical reactions that caused dissolution of apatite (acid generation through re-oxidation of pyrite) did require oxygen to proceed. Thus, even though the described phosphate beds are hosted by a black shale unit that traditionally was thought to reflect an anoxic ocean (e.g., Ettensohn, 1992; Rimmer, 2004) the combined evidence of strong currents, multiple high energy events, and oxygen requiring diagenetic reactions suggest that the overlying waters were more likely suboxic to dysoxic (e.g., Schieber, 2009).

Acknowledgments

The research is sponsored by the Indiana University Shale Research Consortium (Anadarko, Chevron, ConocoPhillips, ExxonMobil, Shell, Statoil, Marathon, Whiting, and Wintershall). An NSF grant to Juergen Schieber (EAR-0318769) provided funds for the purchase of the analytical SEM that was used for acquiring the figures used in this study. The authors would like to acknowledge China Scholar Council (CSC) for providing student support. Thanks would go to Dr. Brian Jones and the anonymous reviewer for their constructive suggestions. We also thank Dr. Maria Mastalerz for identification of organic macerals.

References

- Acomb, B., 1979. The petrology, stratigraphy and origin of phosphatic nodules in Upper Devonian and Lower Mississippian rocks of the eastern interior [Thesis], University of Cincinnati unknown p.
- Algeo, T.J., Maynard, J.B., 2004. Trace-element behavior and redox facies in core shales of Upper Pennsylvanian Kansas-type cyclothems. *Chemical Geology* 206 (3–4), 289–318.
- Arning, E.T., Birgel, D., Brunner, B., Peckmann, J., 2009. Bacterial formation of phosphatic laminites off Peru. *Geobiology* 7 (3), 295–307.
- Aumont, O., Bopp, L., 2006. Globalizing results from ocean in situ iron fertilization studies. *Global Biogeochemical Cycles* 20 (2).
- Bailey, J.V., Joye, S.B., Kalanetra, K.M., Flood, B.E., Corsetti, F.A., 2007. Evidence of giant sulphur bacteria in Neoproterozoic phosphorites. *Nature* 445 (7124), 198–201.
- Bailey, J.V., et al., 2013. Filamentous sulfur bacteria preserved in modern and ancient phosphatic sediments: implications for the role of oxygen and bacteria in phosphogenesis. *Geobiology* 11 (5), 397–405.
- Barale, L., D'Atri, A., Martire, L., 2013. The role of microbial activity in the generation of Lower Cretaceous Mixed Fe-oxide-phosphate ooids from the Provencal Domain, French Maritime Alps. *Journal of Sedimentary Research* 83 (2), 196–206.
- Baturin, G.N., 1982. Phosphorites on the Sea Floor. Elsevier.
- Baturin, G., 1999. Hypotheses of phosphogenesis and oceanic environment. *Lithology and Mineral Resources C (C of Litologiya i Poleznye Iskopaemye)* 34, 411–430.
- Benzerara, K., et al., 2004. Biologically controlled precipitation of calcium phosphate by *Ramlibacter tataouinensis*. *Earth and Planetary Science Letters* 228 (3–4), 439–449.
- Berner, R.A., 1973. Phosphate removal from sea water by adsorption on volcanogenic ferric oxides. *Earth and Planetary Science Letters* 18 (1), 77–86.
- Berner, R.A., 1980. *Early Diagenesis: A Theoretical Approach*. Princeton Series in Geochemistry. Princeton University Press, Princeton.
- Blake, R., O'Neil, J., Garcia, G., 1998. Effects of microbial activity on the delta 18O of dissolved inorganic phosphate and textural features of synthetic apatites. *American Mineralogist* 83 (11–12 Part 2), 1516–1531.
- Blakey, R., 2005. Late Devonian (360 Ma), North American Paleogeography. Colorado Plateau Geosystems, Inc.
- Brezinski, D.K., Cecil, C.B., Skema, V.W., Stamm, R., 2008. Late Devonian glacial deposits from the eastern United States signal an end of the mid-Paleozoic warm period. *Palaeogeography Palaeoclimatology Palaeoecology* 268 (3–4), 143–151.
- Brezinski, D.K., Cecil, C.B., Skema, V.W., 2009. Late Devonian glaciogenic and associated facies from the central Appalachian Basin, eastern United States. *Geological Society of America Bulletin* 122 (1–2), 265–281.
- Briggs, D.E., Wilby, P.R., 1996. The role of the calcium carbonate-calcium phosphate switch in the mineralization of soft-bodied fossils. *Journal of the Geological Society* 153 (5), 665–668.
- Burnett, W.C., 1977. Geochemistry and origin of phosphorite deposits from off Peru and Chile. *Geological Society of America Bulletin* 88 (6), 813–823.
- Byrne, R.H., Liu, X., Schifj, J., 1996. The influence of phosphate coprecipitation on rare earth distributions in natural waters. *Geochemica et Cosmochimica Acta* 60 (17), 3341–3346.
- Calvert, S.E., Pedersen, T.F., 1993. Geochemistry of recent oxic and anoxic marine sediments—implications for the geological record. *Marine Geology* 113 (1–2), 67–88.
- Caputo, M.V., de Melo, J.H.G., Streel, M., Isbell, J.L., 2008. Late Devonian and early Carboniferous glacial records of South America. *Geological Society of America Special Papers* 441, 161–173.
- Christoffersen, J., 1981. Dissolution of calcium hydroxyapatite. *Calcified Tissue International* 33 (1), 557–560.
- Conant, L.C., Swanson, V.E., 1961. Chattanooga Shale and related rocks of central Tennessee and nearby areas. *Geological Survey Professional Paper* 357.
- Cook, P., O'Brien, G.W., 1990. Neogene to Holocene phosphorites of Australia. In: Burnett, W.C., Riggs, S.R. (Eds.), *Phosphate Deposits of the World Neogene to Modern Phosphorite vol. 3*. Cambridge University Press, Cambridge, pp. 98–115.
- Cosmidis, J., et al., 2013. Nanometer-scale characterization of exceptionally preserved bacterial fossils in Paleocene phosphorites from Ouled Abdoun (Morocco). *Geobiology* 11 (2), 139–153.
- Crusius, J., Calvert, S., Pedersen, T., Sage, D., 1996. Rhenium and molybdenum enrichments in sediments as indicators of oxic, suboxic and sulfidic conditions of deposition. *Earth and Planetary Science Letters* 145 (1), 65–78.
- de Baar, H.J., de Jong, J.T., 2001. Distributions, sources and sinks of iron in seawater. *The Biogeochemistry of Iron in Seawater* pp. 123–253.
- de Witt, W., Roen, Jr., J.B., and Wallace, L.G., 1993. Stratigraphy of Devonian black shales and associated rocks in the Appalachian basin. *U.S. Geological Survey Bulletin* 1909-B, B1–B57.
- Dickinson, J.A., Wallace, M.W., 2009. Phosphate-rich deposits associated with the Mio-Pliocene unconformity in south-east Australia. *Sedimentology* 56 (2), 547–565.
- Dix, G.R., Mullins, H.T., 1987. Shallow, subsurface growth and burial alteration of Middle Devonian calcite concretions. *Journal of Sedimentary Research* 57 (1).
- Dornbos, S.Q., 2011. *Phosphatization through the Phanerozoic*. Taphonomy. Springer, Netherlands, pp. 435–456.
- Dornbos, S.Q., et al., 2006. Environmental controls on the taphonomy of phosphatized animals and animal embryos from the Neoproterozoic Doushantuo Formation, Southwest China. *Palaaios* 21 (1), 3–14.
- Dorozhkin, S.V., 2002. A review on the dissolution models of calcium apatites. *Progress in Crystal Growth and Characterization of Materials* 44 (1), 45–61.
- Dorozhkin, S.V., 2012. Dissolution mechanism of calcium apatites in acids: a review of literature. *World Journal of Methodology* 2 (1), 1–17.
- Elderfield, H., Greaves, M.J., 1982. The rare-earth elements in sea-water. *Nature* 296 (5854), 214–219.
- Emerson, S.R., Huested, S.S., 1991. Ocean anoxia and the concentrations of molybdenum and vanadium in seawater. *Marine Chemistry* 34 (3), 177–196.

- Erik, P.K., Bynum, J., 2014. Regional Upwelling During Late Devonian Woodford Deposition in Oklahoma and Its Influence on Hydrocarbon Production and Well Completion. AAPG Education Directorate Woodford Shale Forum. AAPG, Oklahoma City.
- Ettensohn, F.R., 1985. Controls on development of Catskill Delta complex basin-facies. Geological Society of America Special Papers 201, 65–78.
- Ettensohn, F.R., 1992. Controls on the origin of the Devonian–Mississippian oil and gas shales, east-central United States. *Fuel* 71 (12), 1487–1492.
- Filippelli, G.M., 1997. Controls on phosphorus concentration and accumulation in oceanic sediments. *Marine Geology* 139 (1–4), 231–240.
- Follmi, K.B., 1996. The phosphorus cycle, phosphogenesis and marine phosphate-rich deposits. *Earth-Science Reviews* 40 (1–2), 55–124.
- Follmi, K.B., Gertsch, B., Renevey, J.P., De Kaenel, E., Stille, P., 2007. Stratigraphy and sedimentology of phosphate-rich sediments in Malta and south-eastern Sicily (latest Oligocene to early Late Miocene). *Sedimentology* 55 (4), 1029–1051.
- Froelich, P.N., et al., 1979. Early oxidation of organic matter in pelagic sediments of the eastern equatorial Atlantic: suboxic diagenesis. *Geochimica et Cosmochimica Acta* 43 (7), 1075–1090.
- Froelich, P.N., Bender, M.L., Luedtke, N.A., 1982. The marine phosphorus cycle. *American Journal of Science* 282 (4), 474–511.
- Glenn, C.R., et al., 1994. Phosphorus and phosphorites: sedimentology and environments of formation. *Eclogae Geologicae Helveticae* 87 (3), 747–788.
- Habermann, D., et al., 2000. High resolution rare-earth elements analyses of natural apatite and its application in geo-sciences: combined micro-PIXE, quantitative CL spectroscopy and electron spin resonance analyses. *Nuclear Instruments and Methods in Physics Research Section B: Beam Interactions with Materials and Atoms* 161–163, 846–851.
- Hannigan, R.E., Sholkovitz, E.R., 2001. The development of middle rare earth element enrichments in freshwaters: weathering of phosphate minerals. *Chemical Geology* 175 (3–4), 495–508.
- Heggie, D.T., et al., 1990. Organic carbon cycling and modern phosphorite formation on the East Australian continental margin: an overview. Geological Society, London, Special Publications 52 (1), 87–117.
- Helz, G., et al., 1996. Mechanism of molybdenum removal from the sea and its concentration in black shales: EXAFS evidence. *Geochimica et Cosmochimica Acta* 60 (19), 3631–3642.
- Hirschler, A., Lucas, J., Hubert, J.C., 1990. Apatite genesis: a biologically induced or biologically controlled mineral formation process? *Geomicrobiology Journal* 8 (1), 47–56.
- Holmer, L.E., 1989. Middle Ordovician Phosphatic Inarticulate Brachiopods from Västergötland and Dalarna, Sweden.
- Huerta-Diaz, M.A., Morse, J.W., 1990. A quantitative method for determination of trace metal concentrations in sedimentary pyrite. *Marine Chemistry* 29, 119–144.
- Ingall, E.D., Cappellen, P.V., 1990. Relation between sedimentation rate and burial of organic phosphorus and organic carbon in marine sediments. *Geochimica et Cosmochimica Acta* 54 (2), 373–386.
- Isaacson, P.E., et al., 2008. Late Devonian–earliest Mississippian glaciation in Gondwanaland and its biogeographic consequences. *Palaeogeography Palaeoclimatology Palaeoecology* 268 (3–4), 126–142.
- Jarvis, I., 1995. Phosphorite geochemistry: state-of-the-art and environmental concerns. *Eclogae Geologicae Helveticae* 87 (3), 656–664.
- Johnson, J.G., Sandberg, C.A., 1989. Devonian eustatic events in the western United States and their biostratigraphic responses. In: McMillan, N.J., et al. (Eds.), *Devonian of the world*. Paleontology, Paleogeology, and Biostratigraphy. Canadian Society of Petroleum Geologists Memoir Volume III. Canadian Society of Petroleum, pp. 171–178.
- Johnson, J.G., Sandberg, C.A., Poole, F.G., 1989. Early and Middle Devonian paleogeography of western United States. In: McMillan, N.J., et al. (Eds.), *Devonian of the world*. Regional Syntheses: Canadian Society of Petroleum Geologists Memoir Volume I, pp. 161–182.
- Johnson, J.G., Sandberg, C.A., Poole, F.G., 1991. Devonian lithofacies of western United States. In: Cooper, J.D., Steven, C.H. (Eds.), *Paleozoic Paleogeography of the western United States II: Pacific Section*. Society of Economic Paleontologists and Mineralogists, pp. 83–105.
- Kaufmann, B., 2006. Calibrating the Devonian Time Scale: a synthesis of U–Pb ID–TIMS ages and conodont stratigraphy. *Earth-Science Reviews* 76 (3–4), 175–190.
- Kazakov, A.V., 1937. The phosphorite facies and the genesis of phosphorite. *Transactions of the Science Institute of Fertilizers and Insecto-fungicides* 142, 95–113.
- Kempe, U., Götze, J., 2002. Cathodoluminescence (CL) behaviour and crystal chemistry of apatite from rare-metal deposits. *Mineralogical Magazine* 66 (1), 151–172.
- Kidder, D.L., 1985. Petrology and origin of phosphate nodules from the Midcontinent Pennsylvanian epicontinental sea. *Journal of Sedimentary Research* 55 (6).
- Kouchinsky, A., Bengtson, S., Gershwin, L.-a., 1999. Cnidarian-like embryos associated with the first shelly fossils in Siberia. *Geology* 27 (7), 609–612.
- Krom, M.D., Berner, R.A., 1981. The diagenesis of phosphorus in a nearshore marine sediment. *Geochimica et Cosmochimica Acta* 45 (2), 207–216.
- Lancelot, C., et al., 2009. Spatial distribution of the iron supply to phytoplankton in the Southern Ocean: a model study. *Biogeosciences* 6 (12), 2861–2878.
- Lazar, O.R., 2007. Redefinition of the New Albany Shale of the Illinois Basin: An Integrated, Stratigraphic, Sedimentologic, and Geochemical Study. ProQuest.
- Lepland, A., et al., 2013. Potential influence of sulphur bacteria on Palaeoproterozoic phosphogenesis. *Nature Geoscience* 7 (1), 20–24.
- Lucas, J., Prevot, L.E., 1991. Phosphates and fossil preservation. In: Allison, P.A., Briggs, D.E.G. (Eds.), *Taphonomy: Releasing the Data Locked in the Fossil Record*. Plenum, New York.
- Lyons, T.W., Severmann, S., 2006. A critical look at iron paleoredox proxies: new insights from modern euxinic marine basins. *Geochimica et Cosmochimica Acta* 70 (23), 5698–5722.
- Lyons, P.C., et al., 1990. The laser microprobe mass analyzer for determining partitioning of minor and trace-elements among intimately associated macerals—an example from the Swallow Wood Coal Bed, Yorkshire, UK. *Fuel* 69 (6), 771–775.
- McArthur, J.M., Coleman, M.L., Bremner, J.M., 1980. Carbon and oxygen isotopic composition of structural carbonate in sedimentary francolite. *Journal of the Geological Society* 137 (6), 669–673.
- McKelvey, V.E., 1959. Geology of Permian Rocks in the Western Phosphate Field; The Phosphoria, Park City, and Sheshhorn Formations in the Western Phosphate Field (313A).
- McLennan, S., 1989. Rare earth elements in sedimentary rocks; influence of provenance and sedimentary processes. *Reviews in Mineralogy and Geochemistry* 21 (1), 169–200.
- Moore, J.K., Braucher, O., 2008. Sedimentary and mineral dust sources of dissolved iron to the world ocean. *Biogeosciences* 5 (3), 631–656.
- Morad, S., Alaasm, I.S., 1994. Conditions of formation and diagenetic evolution of Upper Proterozoic phosphate nodules from Southern Sweden—evidence from petrology, mineral chemistry and isotopes. *Sedimentary Geology* 88 (3–4), 267–282.
- Murray, R.W., Buchholtz Ten Brink, M.R., Gerlach, D.C., Russ Iii, G.P., Jones, D.L., 1991. Rare earth, major, and trace elements in chert from the Franciscan Complex and Monterey Group, California: assessing REE sources to fine-grained marine sediments. *Geochimica et Cosmochimica Acta* 55 (7), 1875–1895.
- Nemliher, J., Kurvits, T., Kallaste, T., et al., 2004. Apatite varieties in the shell of the Cambrian lingulate brachiopod *Obolus apollinis* Eichwald[C]. *Proceedings of the Estonian Academy of Sciences, Geology* 53(4).
- O'brien, G., et al., 1990. Sedimentation dynamics and redox iron-cycling: controlling factors for the apatite–glauconite association on the East Australian continental margin. Geological Society, London, Special Publications 52 (1), 61–86.
- Over, D.J., 2007. Conodont biostratigraphy of the Chattanooga Shale, Middle and Upper Devonian, Southern Appalachian Basin, Eastern United States. *Journal of Paleontology* 81 (6), 1194–1217.
- Over, D.J., Lazar, R., Baird, G.C., Schieber, J., Ettensohn, F.R., 2009. Protosalvinia Dawson and associated conodonts of the upper trachytera zone, Famennian, Upper Devonian, in the eastern United States. *Journal of Paleontology* 83 (1).
- Palmer, C.A., Lyons, P.C., 1990. Chemistry and origin of minor and trace-elements in selected vitrinite concentrates from bituminous and anthracitic coals. *International Journal of Coal Geology* 16 (1–3), 189–192.
- Pareek, H.S., Bardhan, B., 1985. Trace-elements and their variation along seam profiles of certain coal seams of Middle and Upper Barakar Formations (Lower Permian) in East Bokaro Coalfield, District Hazaribagh, Bihar, India. *International Journal of Coal Geology* 5 (3), 281–314.
- Parrish, J.T., 1982. Upwelling and petroleum source beds, with reference to Paleozoic. *AAPG Bulletin* 66 (6), 750–774.
- Petsch, S.T., Berner, R.A., 1998. Coupling the geochemical cycles of C, P, Fe, and S: the effect on atmospheric O₂ and the isotopic records of carbon and sulfur. *American Journal of Science* 298 (3), 246–262.
- Piper, D.Z., 1994. Seawater as the source of minor elements in black shales, phosphorites and other sedimentary rocks. *Chemical Geology* 114 (1), 95–114.
- Piper, D.Z., Link, P.K., 2002. An upwelling model for the Phosphoria Sea: a Permian, ocean-margin sea in the northwest United States. *AAPG Bulletin* 86 (7).
- Porter, K.G., Robbins, E.I., 1981. Zooplankton fecal pellets link fossil fuel and phosphate deposits. *Science* 212 (4497), 931–933.
- Potter, P.E., Maynard, J.B., Pryor, W.A., 1982. Appalachian gas bearing Devonian shales—statements and discussions. *Oil & Gas Journal* 80 (4), 290–318.
- Poulton, S.W., Raiswell, R., 2002. The low-temperature geochemical cycle of iron: from continental fluxes to marine sediment deposition. *American Journal of Science* 302 (9), 774–805.
- Puura, J., Lang, L., 2013. Phosphatized organic nanostructures in the Cambrian linguloid brachiopod *Ungula inornata* (Mickwitz). *Estonian Journal of Earth Sciences* 62 (3), 121.
- Raiswell, R., 1976. The microbiological formation of carbonate concretions in the Upper Lias of NE England. *Chemical Geology* 18 (3), 227–244.
- Raiswell, R., 1997. A geochemical framework for the application of stable sulphur isotopes to fossil pyritization. *Journal of the Geological Society* 154 (2), 343–356.
- Raiswell, R., 2011. Iron transport from the continents to the open ocean: the aging-rejuvenation cycle. *Elements* 7 (2), 101–106.
- Raiswell, R., et al., 2006. Contributions from glacially derived sediment to the global iron (oxyhydr)oxide cycle: implications for iron delivery to the oceans. *Geochimica et Cosmochimica Acta* 70 (11), 2765–2780.
- Reaves, C.M., 1986. Organic matter metabolizability and calcium carbonate dissolution in nearshore marine muds. *Journal of Sedimentary Research* 56 (4).
- Reimers, C., Kastner, M., Garrison, R., 1990. The role of bacterial mats in phosphate mineralization with particular reference to the Monterey Formation. *Phosphate Deposits of the World* 3, 300–311.
- Richter, D.K., Gotte, T., Gotze, J., Neuser, R.D., 2003. Progress in application of cathodoluminescence (CL) in sedimentary petrology. *Mineralogy and Petrology* 79 (3–4), 127–166.
- Rimmer, S.M., 2004. Geochemical paleoredox indicators in Devonian–Mississippian black shales, central Appalachian basin (USA). *Chemical Geology* 206 (3–4), 373–391.
- Rimmer, S.M., Thompson, J.A., Goodnight, S.A., Robl, T.L., 2004. Multiple controls on the preservation of organic matter in Devonian–Mississippian marine black shales: geochemical and petrographic evidence. *Palaeogeography Palaeoclimatology Palaeoecology* 215 (1–2), 125–154.
- Robl, T.L., Rimmer, S.M., Barron, L.S., 1992. Organic petrography of Mississippian and Devonian shales in east-central Kentucky. *Fuel* 71 (3), 267–271.
- Roen, J.B., 1983. Geology of the Devonian black shales of the Appalachian Basin.
- Sageman, B.B., et al., 2003. A tale of shales: the relative roles of production, decomposition, and dilution in the accumulation of organic-rich strata, Middle–Upper Devonian, Appalachian basin. *Chemical Geology* 195 (1–4), 229–273.

- Sandberg, C.A., Morrow, J.R., Ziegler, W., 2002. Late Devonian sea-level changes, catastrophic events, and mass extinctions. *Special Paper of the Geological Society of America* 473–488.
- Schieber, J., 1994a. Evidence for high-energy events and shallow-water deposition in the Chattanooga Shale, Devonian, Central Tennessee, USA. *Sedimentary Geology* 93 (3–4), 193–208.
- Schieber, J., 1994b. Paleoflow Patterns and Macroscopic Sedimentary Features in the Late Devonian Chattanooga Shale of Tennessee: Differences Between the Western and Eastern Appalachian Basin.
- Schieber, J., 1996. Early diagenetic silica deposition in algal cysts and spores: a source of sand in black shales? *Journal of Sedimentary Research* 66 (1).
- Schieber, J., 1998. Sedimentary features indicating erosion, condensation, and hiatuses in the Chattanooga Shale of Central Tennessee: relevance for sedimentary and stratigraphic evolution, Shales and mudstones. *Basin Studies, Sedimentology, and Paleontology Volume I*. E. Schweizerbart'sche Verlagsbuchhandlung, Stuttgart, pp. 187–215.
- Schieber, J., 2003. Simple gifts and buried treasures—implications of finding bioturbation and erosion surfaces in black shales. *The Sedimentary Record* 1 (2), 4–8.
- Schieber, J., 2007. Oxidation of detrital pyrite as a cause for Marcasite Formation in marine lag deposits from the Devonian of the eastern US. *Deep Sea Research Part II: Topical Studies in Oceanography* 54 (11–13), 1312–1326.
- Schieber, J., 2009. Discovery of agglutinated benthic foraminifera in Devonian black shales and their relevance for the redox state of ancient seas. *Palaeogeography Palaeoclimatology Palaeoecology* 271 (3), 292–300.
- Schieber, J., 2011. Marcasite in black shales—a mineral proxy for oxygenated bottom waters and intermittent oxidation of Carbonaceous muds. *Journal of Sedimentary Research* 81 (7), 447–458.
- Schieber, J., Baird, G., 2001. On the origin and significance of pyrite spheres in Devonian black shales of North America. *Journal of Sedimentary Research* 71 (1), 155–166.
- Schieber, J., Lazar, R.O., 2004. Devonian black shales of the Eastern U.S.: new insights into sedimentology and stratigraphy from the subsurface and outcrops in the Illinois and Appalachian Basins. *Indiana Geological Survey Open File Study 04-05. Field Guide for the 2004 Great Lakes Section SEPM Annual Field Conference*.
- Schieber, J., Lazar, R., 2010. Outcrop description, Central Kentucky (Stops 7–9). In: Schieber, J., Lazar, R., Bohacs, K. (Eds.), *Sedimentology and stratigraphy of shales: expression and correlation of depositional sequences in the Devonian of Tennessee, Kentucky and Indiana. Field Guide for Post-Convention Field Trip 10. AAPG 2010 Annual Convention in New Orleans*, pp. 116–142.
- Schieber, J., Riciputi, L., 2005. Pyrite and marcasite coated grains in the Ordovician Winnipeg Formation, Canada: an intertwined record of surface conditions, stratigraphic condensation, geochemical “reworking,” and microbial activity. *Journal of Sedimentary Research* 75 (5), 907–920.
- Schieber, J., Krinsley, D., Riciputi, L., 2000. Diagenetic origin of quartz silt in mudstones and implications for silica cycling. *Nature* 406 (6799), 981–985.
- Schieber, J., Southard, J.B., Thaisen, K., 2007. Accretion of Mudstone Beds from Migrating Floccule Ripples. *Science* 318, 1760–1763.
- Schieber, J., Lazar, R., Bohacs, K., 2010. Sedimentology and stratigraphy of shales: expression and correlation of depositional sequences in the Devonian of Tennessee, Kentucky and Indiana. *Field Guide for Post-Convention Field Trip 10. AAPG 2010 Annual Convention in New Orleans*.
- Schulz, H.N., Schulz, H.D., 2005. Large sulfur bacteria and the formation of phosphorite. *Science* 307 (5708), 416–418.
- Sholkovitz, E.R., Landing, W.M., Lewis, B.L., 1994. Ocean particle chemistry: the fractionation of rare earth elements between suspended particles and seawater. *Geochimica et Cosmochimica Acta* 58 (6), 1567–1579.
- Sigel, A., Sigel, H., Sigel, R.K., 2008. *Biom mineralization: From Nature to Application 4*. John Wiley & Sons, Chichester.
- Slatt, R.M., O'Brien, N.R., 2011. Pore types in the Barnett and Woodford gas shales: contribution to understanding gas storage and migration pathways in fine-grained rocks. *AAPG Bulletin* 95 (12), 2017–2030.
- Spears, D., Zheng, Y., 1999. Geochemistry and origin of elements in some UK coals. *International Journal of Coal Geology* 38 (3), 161–179.
- Streel, M., Caputo, M.V., Loboziak, S., Melo, J.H.G., 2000. Late Frasnian–Famennian climates based on palynomorph analyses and the question of the Late Devonian glaciations. *Earth-Science Reviews* 52 (1), 121–173.
- Tagliabue, A., Bopp, L., Aumont, O., 2009. Evaluating the importance of atmospheric and sedimentary iron sources to Southern Ocean biogeochemistry. *Geophysical Research Letters* 36.
- Tappan, H.N., 1980. *The Paleobiology of Plant Protists*. W.H. Freeman, San Francisco.
- Taylor, K.G., Konhauser, K.O., 2011. Iron in earth surface systems: a major player in chemical and biological processes. *Elements* 7 (2), 83–88.
- Taylor, K.G., Macquaker, J.H.S., 2011. Iron minerals in marine sediments record chemical environments. *Elements* 7 (2), 113–118.
- Taylor, S.R., McLennan, S.M., 1985. *The Continental Crust: Its Composition and Evolution*. Blackwell, Oxford.
- Trappe, J., 1998. Phanerozoic phosphorite depositional systems: a dynamic model for a sedimentary resource system. *Lecture Notes in Earth Sciences*. Springer, Berlin; New York (xii, 316 p. pp.).
- Tribovillard, N., Algeo, T.J., Lyons, T., Riboulleau, A., 2006. Trace metals as paleoredox and paleoproductivity proxies: an update. *Chemical Geology* 232 (1–2), 12–32.
- Wang, J., Sharma, A., Tomita, A., 2003. Determination of the modes of occurrence of trace elements in coal by leaching coal and coal ashes. *Energy & Fuels* 17 (1), 29–37.
- Wheat, C.G., Feely, R.A., Mottl, M.J., 1996. Phosphate removal by oceanic hydrothermal processes: an update of the phosphorus budget in the oceans. *Geochimica et Cosmochimica Acta* 60 (19), 3593–3608.
- Wilde, P., Quinby-Hunt, M.S., Erdtmann, B.D., 1996. The whole-rock cerium anomaly: a potential indicator of eustatic sea-level changes in shales of the anoxic facies. *Sedimentary Geology* 101 (1–2), 43–53.